Optical Intensity Control Based on Digital and Analog Systems

Peng Du

Masterarbeit in Physik
angefertigt Institut für Angewandte Physik

vorgelegt der
Mathematisch-Naturwissenschaftlichen Fakultät
der
Rheinischen Friedrich-Wilhelms-Universität
Bonn

August 2018

I hereby declare that this thesis was formulated by myself and that no sources or tools other than those cited were used.

Bonn, ...

Date Signature

1. Gutachter: Prof. Dr. Dieter Meschede
2. Gutachterin: Prof. Dr. Stefan Linden

Contents

CHAPTER 1

Introduction

Discrete-time quantum walks, as the quantum mechanical counterpart of classical random walks, have been proved to possess a profound potential in solving many practical problems. For many oracle situations, quantum walks outperform any classical algorithm with a exponentially faster efficiency[1]. Encouraged by their potential applications, quantum walk experiments have been demonstrated with several physical realizations, including trapped ions[2], cold neutral atoms[3], and photons[4]. As a promising platform of quantum simulation, neutral atoms have several remarkable characteristics. By optical pumping, they can be prepared into well-defined initial state. Besides, two hyperfine states of an atom can be accurately rapidly coupled by microwave radiation. The final states of atoms can be precisely determined from their fluorescence. And many atoms can be trapped in close proximity without affecting each other's quantum states unless they are steered on to do so[5].

In our laboratory, we use cesium atoms, which are trapped in the optical lattices. For the practice of quantum walks, atoms must be well isolated from the noisy environment so that long decoherence time can be achieved. It has been analyzed that fluctuations of the lattice depth originated from intensity fluctuations is one mechanism of decoherence[6] . To suppress the intensity noise of optical lattices, we implement an intensity stabilization control loop based on a field-programmable gate array (FPGA) digital platform (Keysight AIO-H3336F). With the advantages of its integratability and flexibility, the application of digital control opens more possibilities for light intensity modulation. In addition to the intensity stabilization, a feedforward control of light intensity becomes feasible with the use of digital signal processing function of FPGA. The realization of intensity feedforward control provides us with a high bandwidth of intensity modulation as well as the conveniences of creating arbitrary intensity ramp implementation. Therefore, it plays an important role in our exploration into the physics related with a time-varying optical trap depth.

1.1 2D Quantum Walk

In our experimental setup of two-dimensional quantum walks, pre-cooled Cesium atoms are trapped in two-dimensional state-dependent lattices. The source of information in quantum walks is the atomic position at the beginning and end of each measurement. Therefore, to

determine the postition of atoms in the two-dimensional optical lattices, the fluorescence images of trapped atoms are recorded with a high custom designed high numerical aperture objective[7]. The two-dimensional optical lattices provide us with the possibility to implement quantum walks with topologically protected edge states, which have the robustness against spin or spatial dephasing[8].

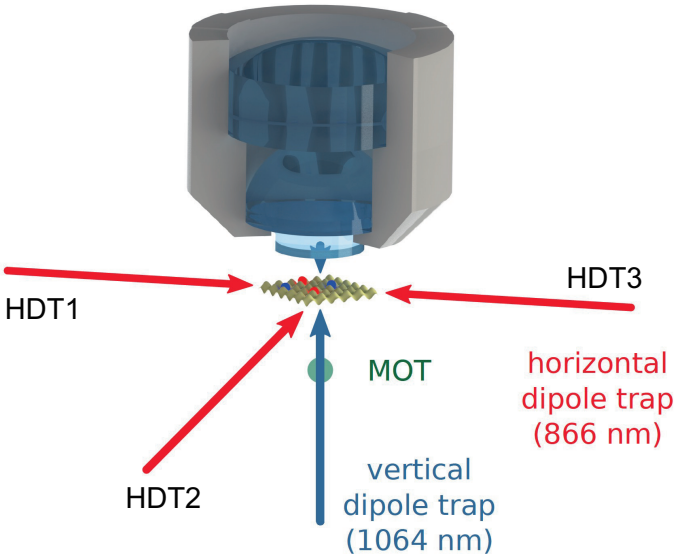

Figure 1.1: The experimental setup of 2D quantum walk[7]. HDT: horizontal dipole trap. MOT: Magneto-optical trap.

To realize quantum walks with neutral atoms, we create a qubit system with two Cesium hyperfine states: $|\uparrow\rangle = |F = 4,\ m_F = 4\rangle$ and $|\downarrow\rangle = |F = 3,\ m_F = 3\rangle$. These two hyperfine states form a pseudo spin-1/2 system, where $|\uparrow\rangle$ state is only attracted by the σ^+-polarized lattice light, while $|\downarrow\rangle$ is predominately attracted by σ^--polarized lattice light [9]. Through Rabi oscillation, the two qubit states can be effectively coupled with a microwave radiation at 9.2 GHz. During the quantum walk experiment, we implement a series of coherent operations with microwave on this two-qubit system. For two-level systems, a general microwave operator can be written down as[10]:

$$\hat{C}(\theta,\phi) = \begin{bmatrix} \cos(\theta/2) & ie^{i\phi}\sin(\theta/2) \\ ie^{-i\phi}\sin(\theta/2) & \cos(\theta/2) \end{bmatrix} \tag{1.1}$$

where specific values of θ and ϕ can be realized by controlling the duration, power and phase of the microwave pulse irradiating the atoms. Mostly used operations are $\theta = \{\pi, \pi/2\}$: a π-pulse can exchange the spin of a non-superposition state ($|\downarrow\rangle \rightarrow |\uparrow\rangle$ and vice versa), while a $\pi/2$ can change non-superposition state into a superposition state $|\uparrow\rangle \rightarrow \frac{1}{\sqrt{2}}(|\uparrow\rangle + |\downarrow\rangle)$ and the other way around[11].

Different microwave operations combined with the shifting of optical lattices are used in the coherent measurements. As one of the key factors of quantum walks, the coherence time of

atoms determines the maximum number of steps we can complete.

1.2 Intensity Stabilization and Coherence of Atoms

The optical lattice potentials are generated from the interaction between neural atoms and laser. When atoms are illuminated with laser beams, a dipole moment in the atoms is induced by the laser electric field, which in turn interacts with the electric field. The interaction potential of the induced dipole moment $\mathbf{p}$ in an oscillating light electric field $\mathbf{E}$ is given by [12]

$$U_{dip}(\mathbf{r}) = -\frac{1}{2}\langle \mathbf{p} \cdot \mathbf{E} \rangle \propto \alpha(\omega_L)\, I(\mathbf{r}) \tag{1.2}$$

where α is the complex polarizability of atoms which depends on laser frequency ω_L. The depth of optical lattices is dependent both on the light intensity I and on the laser frequency ω_L[13]. In reality, laser frequency is usually fixed during the experiment, thus the depth of optical lattices is tunable by the light intensity. In other words, the stabilization of optical depth is realized by stabilizing the optical lattice beam power.

Fluctuations of the lattice depth originate from intensity fluctuations can lead to a spin decoherence[6]. By using the contrast in a Ramsey interferometer[14], the decoherence rate can be described by[6]:

$$p_c = 1 - \exp(-\Delta\Phi^2/2) \approx \Delta\Phi^2/2 \tag{1.3}$$

where the phase variance is determined by the relative intensity noise spectrum, RIN(ω):

$$\Delta\Phi^2 = \frac{\tau^2\eta^2U_0^2}{\bar{h}^2}\int_0^{+\infty} d\omega\, \mathrm{sinc}^2(\omega\tau/2)\mathrm{RIN}(\omega) \tag{1.4}$$

With U_0 being the potential depth at the bottom of the lattice. The formula suggests the low-frequency noise has more obvious influence on the spin coherence. As for the high frequency noise, although it does not undermine the spin coherence much, it does heat atoms up and decrease the surviving time of atom in the optical lattices[9].

1.3 Applications of Fast Intensity Modulation

Although, in the quantum walk experiments, fast intensity modulation is not required, the technique of optical lattice depth modulation has been used for many cold atom experiments. For instance, amplitude modulation has been used to realize the dynamical control of coherent transport of atomic wave packets[15], to perform excitation spectra to characterize the superfluid and the Mott insulating regime[16]. The purpose of our realization of fast intensity modulation lies in the research of the optical control of quantum systems.

CHAPTER 2

Hardware of Intensity Control System

In this chapter, I will give a overview of the intensity control system setup we use in 2D quantum walk experiments. After the introduction of the entire system structure, more detailed information about the key components, namely Keysight FPGA module and Vescent control box will be provided. Through this chapter, I will explain the reason why we apply a digital control platform in our intensity control system.

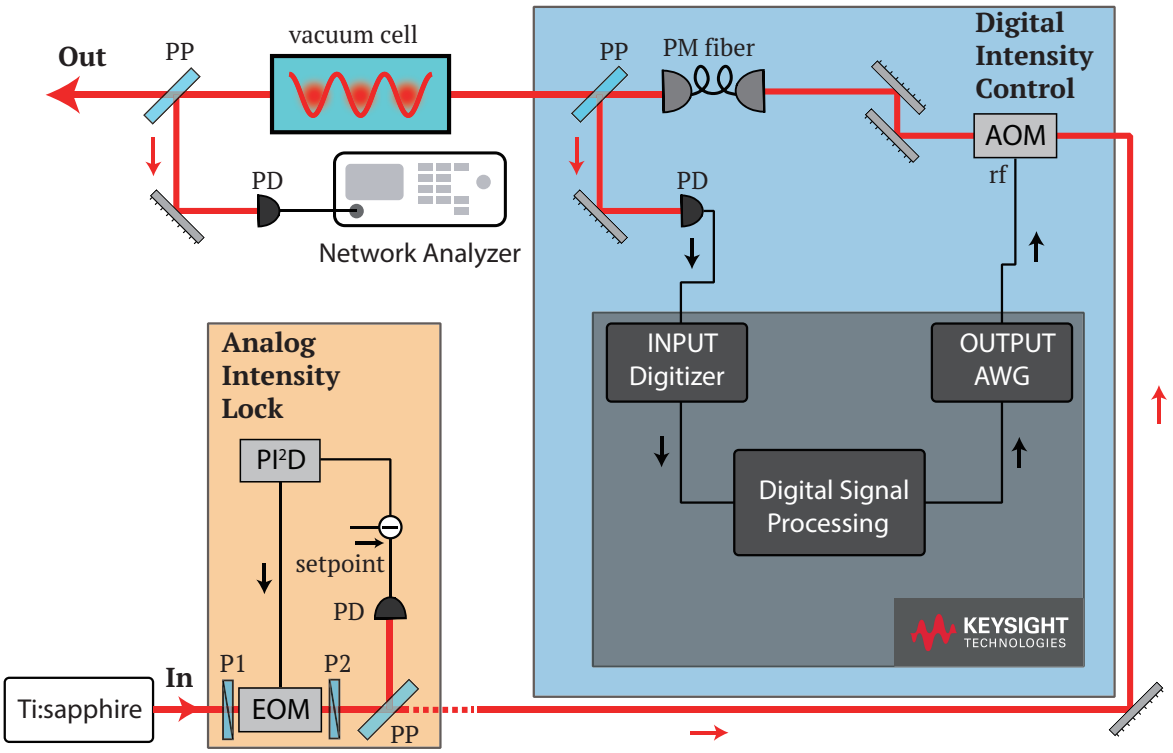

Figure 2.1: Block diagram of entire intensity control system. The part with an orange background is the analog intensity lock, and the part with a blue background is the digital intensity control system. Abbreviations: P1,2: polarizer, EOM: electro-optic modulator, PD: photodiode, PP: pickup plate, rf: radio frequency, PI^2D : proportional-double-integral-derivative controller, AOM: acousto-optic modulator, AWG: arbitrary waveform generator.

2.1 Overview

Shown in Fig. 2.1, the intensity control setup mainly consists of two parts: the digital intensity control part and the analog intensity lock part. The laser beam from the Ti-sapphire laser first goes through the analog intensity lock then modulated by the digital control platform. As for the digital intensity control part, not only executes it the function of intensity stabilization, but it is also used for the fast intensity modulation. With the core component Keysight FPGA module, it possesses the ability to implement many tasks which are very difficult for analog system to perform. However, due to the long delay time of the digital system, the bandwidth of the digital feedback loop is usually limited. In the implementation of intensity stabilization the analog system, which is supposed to have a higher bandwidth, works as a compensation to the digital platform.

2.2 Digital Intensity Control Platform

Digital system, with its continuously improving performance, is winning more and more popularity in different fields of applications. The main advantages of digital system lie in:

- **Flexibility**:
  The digital system can provide users with the possibility to achieve many applications which are difficult for analog system to handle. For example, by adding a lookup table, digital system can easily linearize a non-linear response system. Besides, in a digital feedback loop, it is convenient to realize the dynamic switch on/off of the system, while for the analog system, a complex buffer unit has to be built.

- **Convenience of Programmability**:
  Digital system can be reconfigured for different applications. Unlike analog system, no soldering work needs to be done but only firmware programming.

- **High-speed Data Processing**:
  With the advances in the development of digital signal processing, the operation speed of digital processing of data reaches a high standard. Every cycle of digital processing can only take several ns.

2.2.1 Keysight FPGA Module

Based on the advantages mentioned above, we choose to use the Keysight M3300A module as the core component of our system. The module consists of three main parts: the input ports (digitizers), output ports (arbitrary waveform generators (AWGs)), and the digital signal processing part (FPGA). Experimental data is collected by the digitizers and converted into digital forms. The data is then sent to the digital signal processing part. To have different applications, this FPGA part can be configured into different functional components, for example, PID controller. In the end, the processed data is guided to the AWGs to shape the output signals.

Figure 2.2: Image of the Keysight M3300A module.[17]

General Specification:

Ports	Channel	Sampling Rate	Bits	Bandwidth
Input (Digitizers)	4	500 MSa/s	16	DC - 200 MHz
Output (AWGs)	8	100 MSa/s	14	DC - 100 MHz

Shown in Fig. 2.2, each keysight module has four AWGs and eight digitizers. The AWG outputs have an accuracy of 16 Bits. Within the bandwidth of 200 MHz, it can generate output signals at the maximum sampling rate of 500 M Samples/s. Meanwhile, the digitizers can work with a maximum sampling frequency of 100 MHz with in the input signal bandwidth of 100 MHz. It is noteworthy that the bandwidths of AWGs and digitizers is determined by the bandwidths of digital-to-analog converter (DAC) and analog-to-digital converter ADC components. As for the digital processing speed, a internal reference clock guarantees a cycle period of 10 ns.

AWGs and Signal Modulation

Every Keysight output channel consists of one embedded AWG, one function generator (FG) and modulators. The AWGs thus can be used to generate not only any kind of standard waveform (DC voltages, sinusoidal, square), but also any arbitrary waveform tailed by the user and stored on its onboard random-access memory (RAM).

Shown in Fig. 2.3, in the beginning, the wave shape word is sent to the function generator, while the words of frequency and phase are sent to the angle modulator and the words of amplitude and offset are sent to the amplitude modulator. By using the arbitrary waveform generator inside the output part, we are able to modulate the frequency, phase, amplitude and offset in a desirable way. Take the sinusoidal signal as an example.

During the frequency modulation:

$$Output(t) = A \cdot \cos\left[2\pi\left(f_c + G \cdot AWG(t)\right) \cdot t + \phi_c\right] \tag{2.1}$$

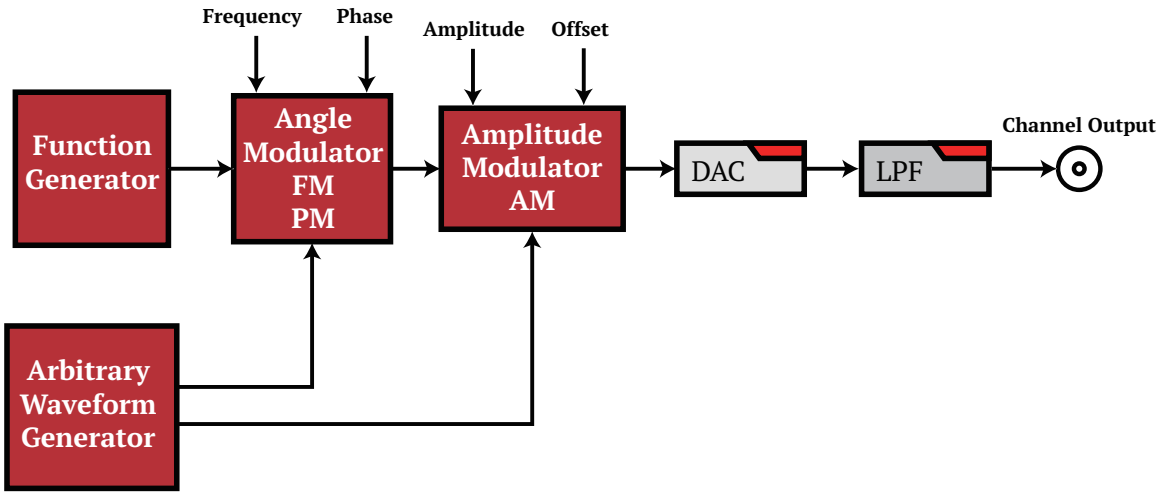

Figure 2.3: Schematics of Keysight module output part. Abbreviations: FM: frequency modulation, PM: phase modulation, AM: amplitude modulation, ADC: analog-digital converter, LPF: low-pass filter.

During the phase modulation:

$$Output(t) = A \cdot \cos\left(2\pi f_c t + G \cdot AWG(t) + \phi_c\right) \tag{2.2}$$

During the amplitude modulation:

$$Output(t) = \left(A + G \cdot AWG(t)\right) \cdot \cos\left(2\pi f_c t + \phi_c\right) \tag{2.3}$$

During the offset modulation:

$$Output(t) = A \cdot \cos\left(2\pi f_c t + \phi_c\right) + G \cdot AWG(t) \tag{2.4}$$

where A is the channel amplitude, G is the deviation gain, $AWG(t)$ is the normalized modulating signal generated by the AWGs, and $\cos(2\pi f_c t + \phi_c)$ is the carrier signal generated by function generator. The generated waveforms can be sent directly to the output, or they can be used as a modulating signal for other modulators.

Digitizers and Data Acquisition (DAQ)

In our intensity control system, the input ports are used to receive the feedback signal from the sensors. Depending on other products' specifications, we can configure the input coupling, the input impedance and the full input scale value. Both DC and AC coupling are available for the input port. As for the impedance, the low input impedance of 50 Ω allows a maximum input voltage to be $[-1.5,\ 1.5]$V, while the high Z mode corresponds to the input voltage range of $[-10,\ 10]$V. To make fully use of the dynamic range of the DAQ part, the full scale of the input can be scaled down to 20% of its original scale by amplifying the input signals. The input signal, after being processed according to the input setting, is sent to the data acquisition part, shown in Fig. 2.4. Then the input information is recorded by the onboard RAM, and further

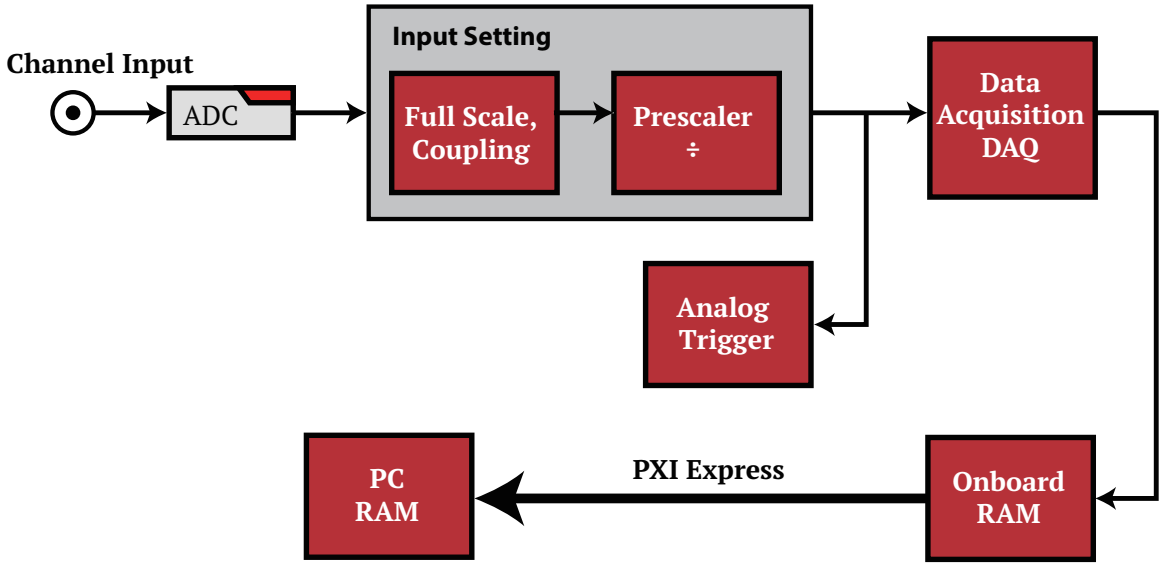

Figure 2.4: Schematics of Keysight module input part. Abbreviations: ADC: analog-digital converter, RAM: random-access memory.

through a PXI express bus, it can be transferred to PC RAM.

FPGA and Digital Signal Processing

FPGAs contain several kinds of basic programmable logic blocks, and a hierarchy of routine resource that allow the blocks to be combined together in a customized manner. Those basic logic blocks can be deliberately configured to perform complex functions, like lookup table or PID controller.

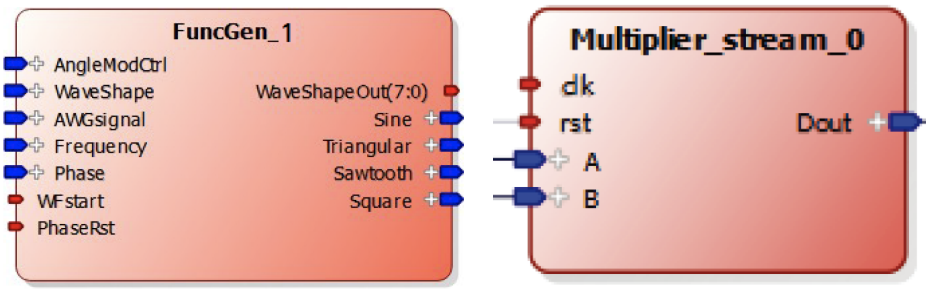

(a) (b)

Figure 2.5: Functional blocks of FPGA (a) hardware block of function generator, (b) multiplier block.

The Keysight module integrates the digitizers and AWGs introduced above with a Xilinx Kintex-7 325T FPGA platform. With the FPGA platform, it is convenient for users to design the digital control system firmware according to the different purposes. Every firmware project of the digital control system is formed by several kinds of functional blocks.

- **Hardware Block**:
  These blocks represent the purchased hardware modules, like function generator, AWG. It can be seen in Fig. 2.5(a), the block includes the input ports of waveshape, frequency, phase, etc, and output ports of sinusoidal, triangular, etc. By connecting those ports with corresponding ports of other blocks, we include this hardware in our firmware project.
- **Library Block**:
  This kind of blocks are very simple and basic, which provide the commonly used FPGA functionality. Shown in Fig. 2.5(b), a multiplier block simply calculates the product of number A and B.
- **User Block**:
  By integrating the basic library blocks, users can create their own functional component, like PID controllers.
- **Vendor Block**:
  This kind of blocks are design and sold by a third party. For those functional components which have a high demand in designing, the FPGA environment provides a solution to integrate the purchased component into user's firmware.

To realize the optical intensity control, we have created our custom firmware by integrating the hardware blocks, the user blocks and the vendor blocks. More details about the structure of intensity control purposed firmware will be introduced in next chapters.

2.2.2 AOM Intensity Modulation

In our system, the amplitude modulation of the optical lattices is realized with acousto-optical modulators (AOMs). Driven by a radio-frequency (RF) signal, AOMs can be used for controlling the power, frequency, or spatial direction of a laser beam through photon-phonon interaction. The amount of light diffracted by the AOM depends on the power of the RF signal. Therefore, the power of the RF signal can be used to modulate the light intensity.

However, barriers towards well-performed intensity modulation system still exist:

- Non-linearity of diffraction efficiency curve: the amount of diffracted light is generally not proportional to the RF signal intensity, which means AOM is a non-linear component when used for intensity modulation. The diffraction efficiency ϵ is determined by the formula[19]:
  $$\epsilon = sin^2\left(\frac{\pi}{2} \cdot \sqrt{P_{in}/P_{sat}}\right) \tag{2.5}$$
  where the P_{in} is the input RF power and P_{sat} is the saturation power.
- Limitation of bandwidth: shown in Fig.2.6, the transient response of AOM indicates that the AOM modulation bandwidth is limited by a deadtime and a rise time of around 257ns and 545 ns respectively[18]. As for the rising part, it should be noted that, for a Gaussian beam, the optical rising time is related with the beam diameter[19]:
  $$\tau_r = 0.65\frac{d}{V} \tag{2.6}$$

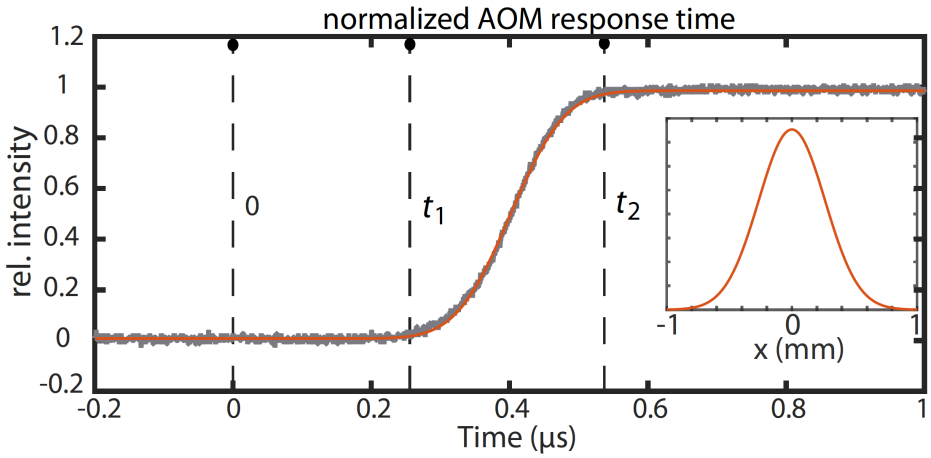

Figure 2.6: [18] AOM step response versus time. The radio frequency signal is switched on instantly at t = 0, and the output of the AOM is measured with a fast photo diode. The dead time of the AOM is indicated by t_1, whereas t_2 denotes the time until the steady state value of of the intensity is reached (rise time). The data is fitted with an error function. Gaussian beam profile calculated from the fitted error function.

Where d is the $1/e^2$ beam diameter and V is the sound velocity. But the narrowing of beam diameter is usually constrained by other conditions.

To overcome the difficulties, we apply a lookup table (LUT) to linearize the response of AOM, and we use a feedforward control mechanism to modulate the optical intensity.

2.3 Analog Intensity Lock

The analog intensity lock is based on the feedback loop formed by an EOM intensity modulator, a sensor (photodiode) and the Vescent control box. It is placed just after the Ti-sapphire laser, supposed to suppress the intensity noise with a higher bandwidth than the digital intensity lock.

2.3.1 EOM Intensity Modulator

Besides AOM, the combination of EOM and polarizers can also make an intensity modulator. The operation of EOM is based on the linear electro-optic effect, which addresses the linear dependence of the refractive index on the electric field strength[20]. If we apply a dc electric field by the electrode attached to the surface of the crystal, the refractive index of two transverse directions will be modified, and the refractive index difference between two directions is proportional to the applied voltage. Therefore, we can modulate the phase difference between the two light electric field components.

The illustration of EOM intensity modulator [21] is shown in Fig. 2.7. Assume the optical axis is along z-direction, and the "fast" and "slow" axis are respectively x'- ,y'- direction. The input polarizer oriented along the x principal axis is aligned at 45° with respect to x' and the

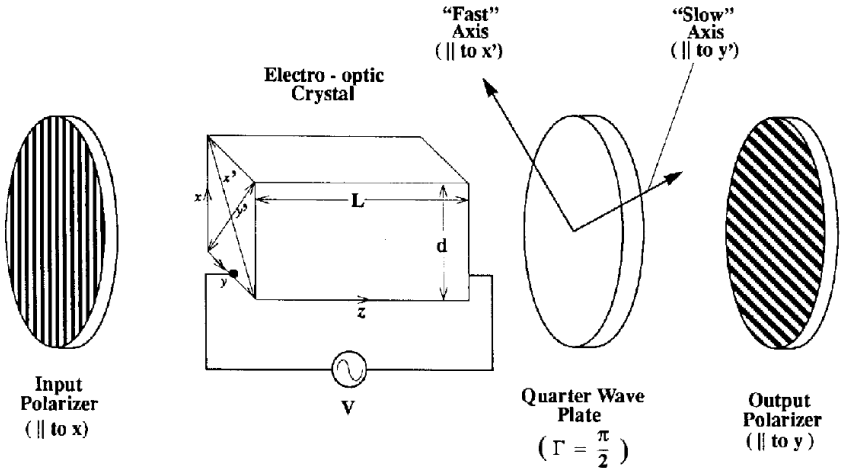

Figure 2.7: Illustration of intensity modulator based on EOM[21].

output polarizer is aligned at a cross position. The optical fields before the output polarizer can be written as:

$$\begin{aligned} E_{x'} &= E_0 \cos(\omega t) \\ E_{y'} &= E_0 \cos\left(\omega t - \phi(V)\right) \end{aligned} \tag{2.7}$$

where $\phi(V)$ is the phase difference introduced by the electro-optic crystal and the quarter wave plate:

$$\phi(V) = \frac{\pi}{2} + \frac{V}{V_\pi} \cdot \pi \tag{2.8}$$

V_π is the half-wave voltage, which produces a phase retardation of π. It can be observed from eq. 2.8, the phase modulation leads to a change of the polarization state, and then the output polarizer subsequently converts this into a change in transmitted optical amplitude and power. Transmission of the modulator is formulated as:

$$T(V) = \sin^2(\frac{\phi}{2}) = \sin^2\left(\frac{\pi}{4} + \frac{\pi V}{2V_\pi}\right) \tag{2.9}$$

The quarter wave plate in this setup is used to add a phase offset so that the transmission is 50% without any applied voltage. In reality, it can be replaced by adding an voltage offset. Because $\sin^2(x)$ function is monotonously increasing throughout the range $[0, \pi]$, it is available to implement the intensity stabilization with EOM intensity modulator.

2.3.2 Vescent Control Box

The Vescent Control Box D2-125 we apply in our analog intensity lock has a slight difference from normal PID controller. It has a second integral part supposed to boost up the control speed. The best feedback bandwidth can be achieved by this control box is 10 MHz[22].

CHAPTER 3

Optical Intensity Stabilization

For the practice of quantum walks, atoms must be well isolated from the noisy environment so that long decoherence time can be achieved. It has been studied by Alberti *et al*[23] that fluctuations of the lattice depth originated from intensity fluctuations is one physical decoherence mechanism. In order to achieve a decent coherence time, we used two intensity locks to suppress the intensity fluctuation of optical lattices as much as possible: one is a digital lock based on AOM intensity modulator, the other one is an analog lock based on electro-optic modulator (EOM) intensity modulator.

In this chapter, I will respectively introduce the two intensity locks used in our experimental, then find the optimal setting of two locks and to evaluate the performance.

3.1 Overview of Feedback Loop

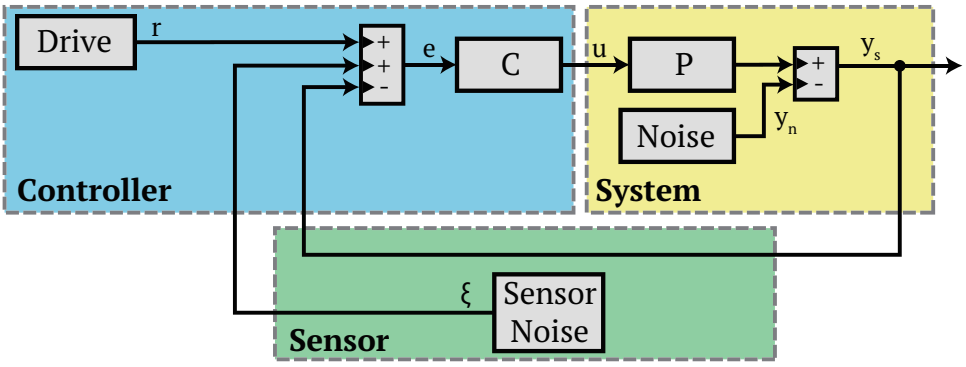

Figure 3.1: The block diagram for feedback control system. C: controller, P: process, r: reference signal, y_n: environmental noises, y_s: system output, ξ: sensor noise, e: error signal, u: controller output.

Feedback loop is widely used in plenty of control systems. By applying the feedback loop's properties, the performance of the system is improved to be more stable and responsive. And the proportional-integral-derivative (PID) controller is the mostly used general-function controller in the filed of feedback control. Heuristically, the terms of a PID controller can be understood

as corresponding to time order: the proportional term is dependent on the ongoing error, the integral term on the accumulation of past errors, and the derivative term is a prediction of future error, based on current rate of change.[24]

In order to analyze the system performance, we build a mathematical model of the feedback loop in frequency domain. The PID controller can be modeled as[25]:

$$C(s) = C_p + \frac{C_i}{s} + C_d s \tag{3.1}$$

where the C_p, C_i and C_d are the proportional, integral, derivative gains need to be tuned according to the particular application. par In a simple situation, we consider the process $P(s)$ as a first-order low-pass filter (the AOM intensity modulator can also be approximately modeled by a low-pass filter with the bandwidth of AOM):

$$P(s) = \frac{G_0(r)}{1 + s/\omega_0} \tag{3.2}$$

where the $G_0(r)$ is the dc gain of process and ω_0 is the bandwidth. If the process is linear, G_0 will be a constant that independent from the reference signal r. For the moment, we neglect the existence of sensor noise, and the dynamics of the system is described by[25]:

$$y(s) = \frac{C(s)P(s)}{1 + C(s)P(s)} r(s) + \frac{1}{1 + C(s)P(s)} y_n(s) \tag{3.3}$$

which means the feedback loop suppresses the environmental disturbance to a factor of $1/(1 + C(s)P(s))$. Therefore, we expect the dc gain of process, G_0, to be as large as possible so that the disturbances can be suppressed to the maximum extent.

Now let the sensor noise come into play:

$$y(s) = \frac{C(s)P(s)}{1 + C(s)P(s)} [r(s) - \xi(s)] + \frac{1}{1 + C(s)P(s)} y_n(s) \tag{3.4}$$

The sensor noise is difficult to be suppressed, because the system has no way to distinguish the measurement noise from the control signal. The tracking error of one feedback loop can be expressed as[25]:

$$e_0(s) = r(s) - y(s) = S(s)[r(s) - d(s)] + T(s)\xi(s) \tag{3.5}$$

where $S(s) = 1/(1 + C(s)P(s))$ denotes the sensitivity function and $T(s) = 1 - S(s) = C(s)P(s)/(1 + C(s)P(s))$ is the complementary sensitivity function. The goal of the feedback loop is to minimize the intensity noise, when the setpoint does not change ($r(s) = 0, \forall s \neq 0$). Since $S(s) + T(s) = 1$, if $S(s)$ is small, the environmental disturbance $d(s)$ will be well rejected, but $T(s)$ will be large and the sensor noise $\xi(s)$ will be fed through the loop and vice versa. For the low-frequency domain, the environment disturbance is usually more significant. For the high-frequency domain, it is possible that beyond a certain frequency, the sensor noise is larger than disturbance. In that case, appropriate lowering the feedback bandwidth by tuning PID gains leads to less noise. Thus, it is important to understand the noises coming from the sensor (including photodiode and Keysight input), and optimize the tradeoff between rejecting

disturbances and suppressing the sensor noises.

3.2 Evaluation of Optical Intensity Stabilization

To evaluate the intensity stabilization performance of the system, we measure the relative intensity noise (RIN) to observe the frequency distribution of noise and calculate the accumulative RIN to obtain the total quantity of intensity noise.

3.2.1 Relative Intensity Noise (RIN)

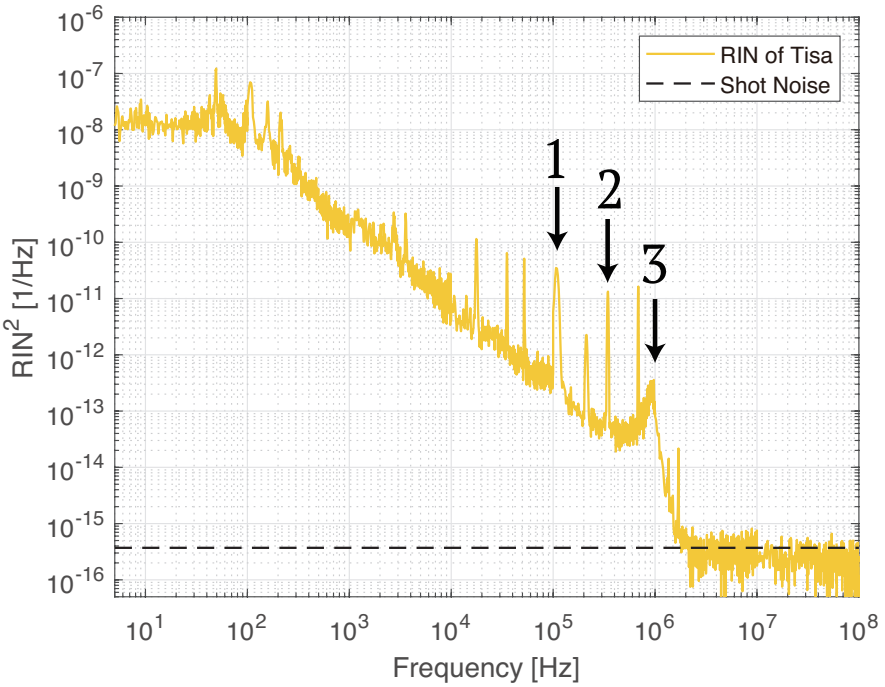

Figure 3.2: RIN of Ti:sapphire laser (Coherent MBR 110), an example of RIN power spectral density.

RIN is the optical power noise normalized to the average power level. The fluctuating optical power of a laser can be written down as[26]

$$P(t) = \bar{P} + \delta P(t) \tag{3.6}$$

where the $\bar{P}$ is the average optical power, and the $\delta P(t)$ is the fluctuation of the optical power over time. The relative noise is obtained by dividing the fluctuation by the average power. And to describe the distribution of the noise over frequency, a power spectral density is used:

$$S_I(f) = \frac{2}{\bar{P}^2} \int_{-\infty}^{+\infty} \langle \delta P(t) \delta P(t+\tau) \rangle \exp(i2\pi f \tau) d\tau \tag{3.7}$$

This power spectral density can measured by a network analzyer (HP 3589A in our case). Fig. 3.2 is the RIN of the Ti:sapphire laser (TiSa) (Coherent MBR 110) we used in our 2D quantum walk experiment. This measurement suggests a fine working status of TiSa. But if there are abnormalities inside the system, by looking at this power spectrum, we can acquire the information about the working status of the components related with TiSa, for example the etalon lock and the power laser.

3.2.2 Cumulative RIN Noise

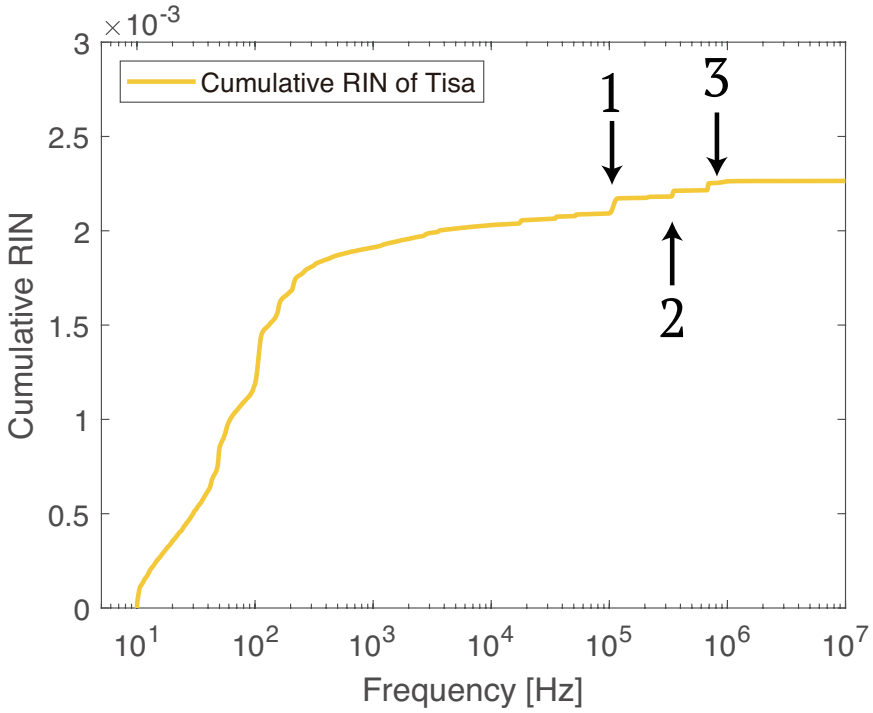

Figure 3.3: Cumulative RIN of Ti:sapphire laser.

Besides the RIN power spectral density, we can also calculate the cumulative RIN of the beam:

$$\frac{\delta P}{\bar{P}}|_{rms} = \sqrt{\int_{f_1}^{f_2} S_I(f)df} \tag{3.8}$$

The cumulative RIN plot provides the total noise quantity over a certain frequency interval. Shown in Fig. 3.3, the relative noise amount of 0.2% from 5 Hz to 10^7 Hz suggests the TiSa is in good working order, according to the specification. Another noteworthy function of the cumulative RIN plot is to evaluate the significance of the noise peaks appearing in RIN power spectral density. For instance, there are eight peaks existing in the frequency interval $[10^4,\ 10^6]$ Hz. From the RIN power spectral density, it is not easy to estimate which of them have more impact on the system. However, from the discreet steps in Fig. 3.3, we can draw the conclusion only three of them are noteworthy with respect to the contribution of the noise quantity.

3.3 Digital Lock Based on Keysight

3.3.1 Overview

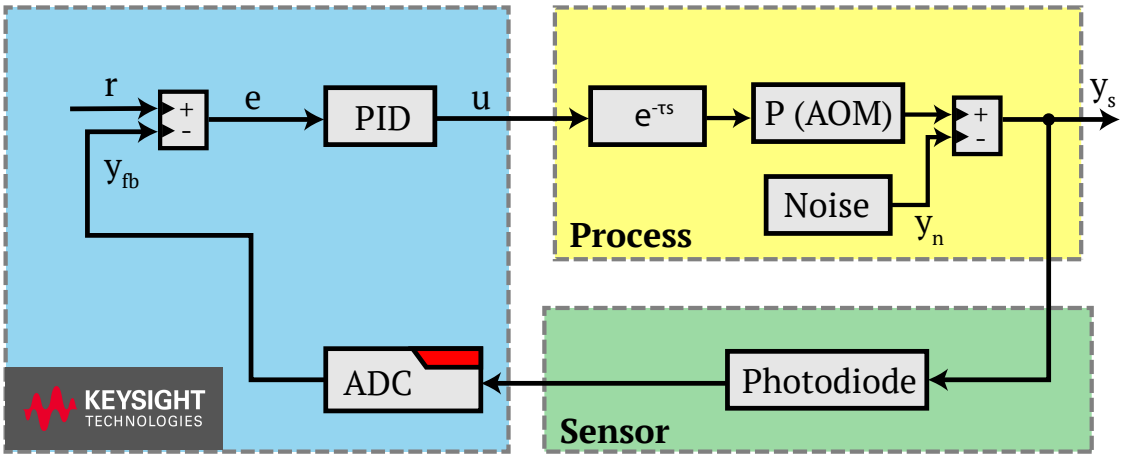

Figure 3.4: Block diagram of digital intensity lock. The digital PID controller is configured within the FPGA platform. Abbreviations: r: reference signal, e: error signal, u: control signal, $e^{-\tau s}$: system delay, P(AOM): process of AOM, ADC: analog-digital converter, y_n: environmental noise, y_{fb}: feedback signal, y_s: output signal.

Shown in Fig. 5.1, the digital intensity lock is formed by Keysight module, AOM and the photodiode as the sensor. Inside the Keysight module, the reference signal provides the setpoint of the feedback loop. Feedback signal measured by photodiode is received by the input port of Keysight module and then subtracted from the reference signal to generate the error. The digital PID controller is custom-configured within the FPGA module. After receiving the error signal, the control signal produced by PID controller is used to drive the AOM.

While the FPGA platform provides users with much flexibility to configure the functional blocks, the time delay accompanied with the complex digital signal processing is inevitable. The system delay $e^{-\tau s}$ includes the dead time of AOM and the delay of digital signal processing inside the FPGA platform. With the delay, the transfer function of the system becomes:

$$y(s) = \frac{C(s)P(s)e^{-\tau s}}{1 + C(s)P(s)e^{-\tau s}}\left[r(s) - \xi(s)\right] + \frac{1}{1 + C(s)P(s)e^{-\tau s}}y_n(s) \tag{3.9}$$

According to control theory, the feedback loop bandwidth is undermined by the existence of the delay. Therefore, we characterize the digital intensity bandwidth by using the step response method, which will be introduced in next subsection.

Another issue coming with the digital system is the readout noise of ADC. As a type of sensor noise, it cannot be suppressed by the feedback loop. To minimize the negative effect of readout noise, we make full use of the dynamic range of the digital system. This measure also enables the system to have a better process gain so that have a better performance in intensity

stabilization.

3.3.2 Characterization of Digital Intensity Lock

Readout Noise of ADC

Although the digital platform provides us with good flexibility, the noise coming from its components can also undermine the quality of the intensity lock. For example, the readout noise of analog-to-digital converters (ADCs), as a part of sensor noise, can be projected to the optical system through the feedback loop and contaminate the control signal. The noise is

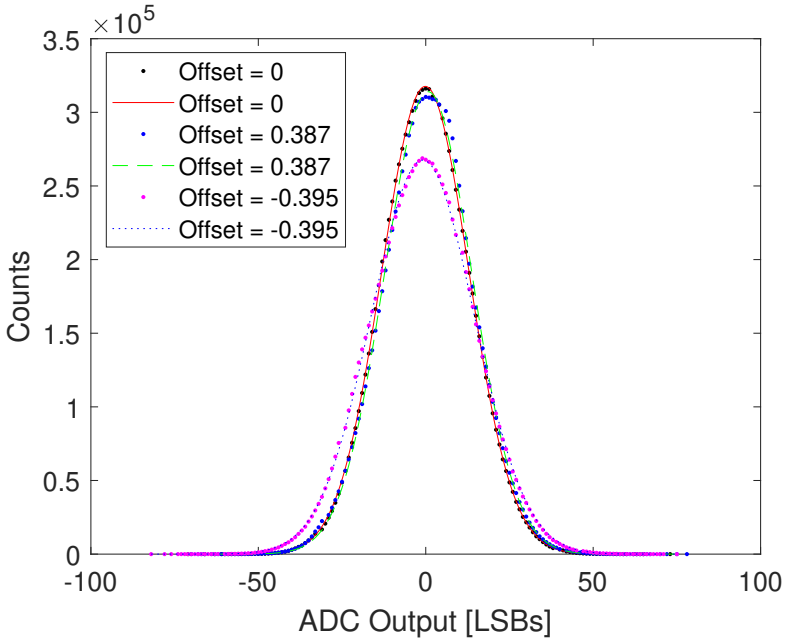

Figure 3.5: Readout noise of ADC at different DC levels.

Offset $[-1, 1]$	0.387	0	-0.395
RMS Noise (LSBs)	13.4	13.4	15.5

Table 3.1: RMS Noise of ADC

characterized by making a statistics of ADC readout with several constant offsets of input. The zero offset is realized by connecting a 50Ω terminating impedance to the input port of Keysight, and the positive and negative offsets are realized with a new cell battery which is supposed to have a very low-noise voltage output. For every voltage, 10^6 readouts are taken and ploted as hitogram. Since the noise is Gaussian, the standard deviation of the histogram, which can be obtained by fitting, corresponds to the effective rms noise. We noticed from Fig. 3.5 that the ADC resolution at positive offset (0.387 V) is almost the same with the one of zero output

(Standard Deviation = 13.4 LSBs), while the negative offset led to a larger standard deviation of 15.5 LSBs. Generally, the non-linear behavior of resolution is not evident, and the effective resolution can be obtained [27] :

$$\begin{aligned} \text{Effective resolution} &= \log_2\left(\frac{2^N}{rms\ Noise}\right) \\ &\approx 10.4 \text{ bits} \end{aligned} \tag{3.10}$$

where N is the total bit number of ADC (14 bits).

From another perspective, we also investigate the spectral distribution of ADC readout noise is also investigated. Taking a time series of 1.6×10^7 readouts from Keysight's digitizer with a 50 Ω terminating impedance connected to the input port , we use Fast Fourier Transform (FFT) algorithm to analyze the RIN contribution from ADC readout noise. The FFT spectrum resolution is given by

$$\text{Frequency Resolution} = \frac{F_s}{N_s} = \frac{100 \text{ MHz}}{16113920} \approx 6.2 \text{ Hz} \tag{3.11}$$

where F_s denotes sampling frequency and N_s denotes the number of sampling points. The frequency upper limit is half of sampling frequency: 50 MHz. This noise spectrum will be compared with measured system RIN spectrum and will be presented in the end of this subsection.

Bandwidth of Digital Lock

The bandwidth of the system can be obtained from the system transfer function $G(s)$. Because the system time response is a convolution of system transfer function and the stimulus signal, if the stimulus signal is a impulse $\delta(t)$, then the system response will be exactly the system transfer function. However, the perfect impulse stimulus is hard to realize, thus an alternative choice would be to apply a Heaviside stimulus, in other words, to measure system step response.

$$\begin{aligned} \mathcal{L}[R'(t)] &= s \cdot \mathcal{L}[\theta(t) * H(t)] \\ &= s \cdot \mathcal{L}[\theta(t)] \cdot \mathcal{L}[H(t)] \\ &= s \cdot \frac{1}{s} \cdot \mathcal{L}[H(t)] \\ &= H(s) \end{aligned} \tag{3.12}$$

It can be seen from the above equation, the Laplace transformation of the derivative of the system step response gives the system transfer function. Since without the LUT this system is nonlinear, we measure the system step response in the following way:

- Apply a minor step of the amplitude of 0.05 from the setpoint level of 0.9, so that the obtained bandwidth corresponds to the setpoint.

- Use a linear transformation to set the beginning level as 0, and the final level as 1. This transformation alter the small step into a standard format.

- For each setting, 10 measurements have been done to reduce the influence of noise. A low-pass filter is applied to reduce the high-frequency noise.

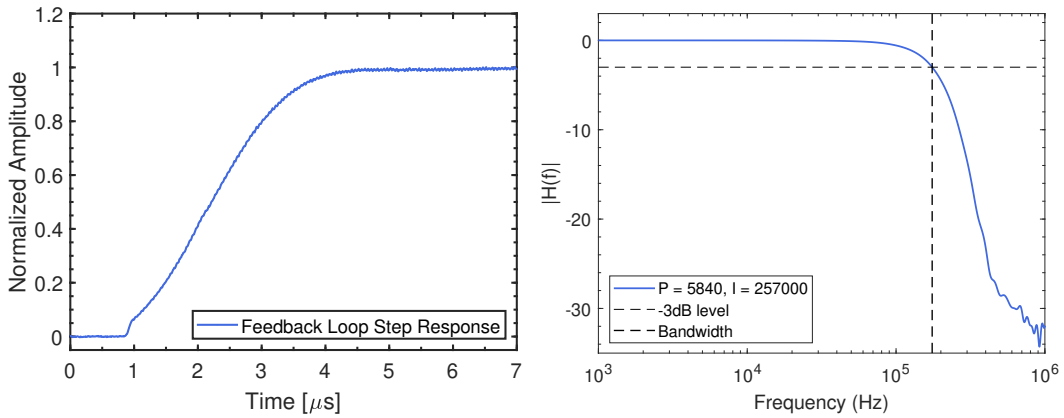

(a) (b)

Figure 3.6: The process to determine the bandwidth of the system. (a) Step response of the digital feedback loop, (b) the amplitude of system transfer function $H(f)$.

An example of the step response is shown in Fig. 3.6(a). At the 0 time point, the trigger signal is applied. After a delay time of around 0.8 μs, the system is driven by the PID controller. It takes another 3 μs for the system to reach level 1. By doing a Fourier transformation to the derivative of the step response data, the amplitude of the transfer function $H(s)$ is plotted in Fig. 3.6(b). With different PID settings, the bandwidths of the system are different. The optimized PID setting according to the rise time and overshooting of step response corresponds to a maximum bandwidth of 170 kHz.

Dynamic Range

It is discussed in the overview part of this chapter, to realize the optimal noise suppression, the dc gain of AOM, G_0, is supposed to be as large as possible. Without the LUT, the intensity stabilization system is a non-linear system, thus G_0 is a function of reference signal r, which is related with the setpoint. Since the proportion of the optical power used for intensity stabilization is adjustable and the modification of the photodiode is also available, we can choose the setpoint regarding the performance of noise suppression. The higher setpoint is used, the more dynamic range we obtain.

Another concern about noise suppression is the sensor noise induced by the ADCs inside Keysight platform. The effective resolution is basically the same throughout the input range. To fully make use of the dynamic range of ADC, it is necessary to have an input signal close to

the input port maximum. Therefore a high setpoint can also benefit the suppression of readout noise.

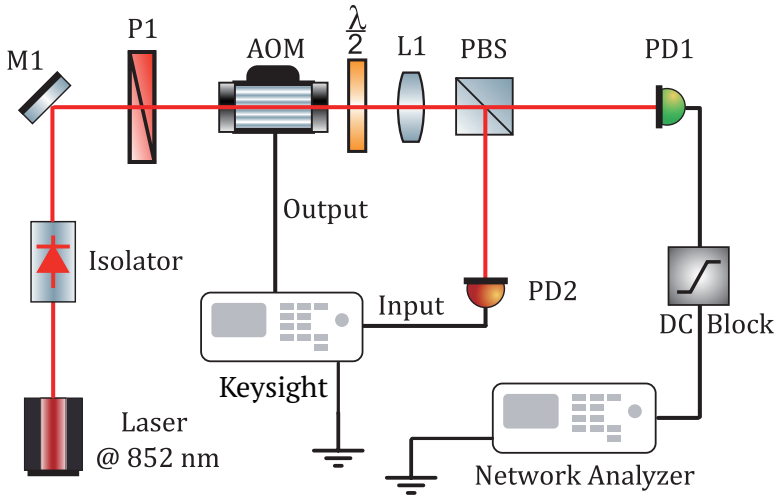

Figure 3.7: Experimental Setup of Out-of-Loop RIN Measurement. Red lines denote the optical path and the black lines denote the electrical connection. PD1: out-of-loop photodiode, PD2: in-loop photodiode, P1: polarizer, $\frac{\lambda}{2}$: half-wave plate, L1: lens used to focus beam at photodiode, PBS: polarized beam splitter.

To evaluate the performance of intensity stabilization with regard to the dynamic range, we measure the out-of-loop RIN of the system. The prototyping RIN measurement setup is shown in Fig. 3.7. We use a diode laser at 852 nm, which has a contiguous wavelength with the TiSa in the 2D quantum walk experiment. It has a comparatively low intensity noise – a cumulative RIN of 6.586×10^{-6}. A combination of half wave plate and polarized beamsplitter helps balance the optical power measured at in-loop and out-of-loop photodiodes. The DC block before the network analyzer filter the signal close to DC so that the input power satisfies the requirement of the network analyzer.

In the RIN measurement, we first measure the noise power spectral density of the system with setpoints at 0.1, 0.3 and 0.9. The DC voltage of the photodiode output gives the average power of the beam. Afterwards, we blocked the out-of-loop photodiode to measure the background noise from the photodiode with the same measuring power range. The direct power unit of network analyzer is of dBm/$\sqrt{\text{Hz}}$. By converting the unit to V^2/Hz, we can subtract the background noise from the RIN of beam. And due to the proportionality between optical power and photodiode output voltage, the spectrum we measure is actually the RIN^2.

The RIN spectrum of three different setpoints is shown in Fig. 3.8. It can be observed that in the frequency domain $[10^1,\ 10^4]$ Hz, three curves are parallel and share the same spacing between the adjacent curves. The situation of setpoint at 0.9 has the smallest RIN, while the RIN^2 of setpoint at 0.3 is approximately 9 times of it. Similarly, the RIN^2 of setpoint at 0.1 is approximately 9 times of the RIN of setpoint at 0.3. According to the Eq. 3.9, if the process gain is three times larger, then the noise suppression effect will be three times stronger, which stays consistent with the measurement result. As for the readout noise, if the input level is three times higher, the RIN contribution from readout noise will be three times less as well.

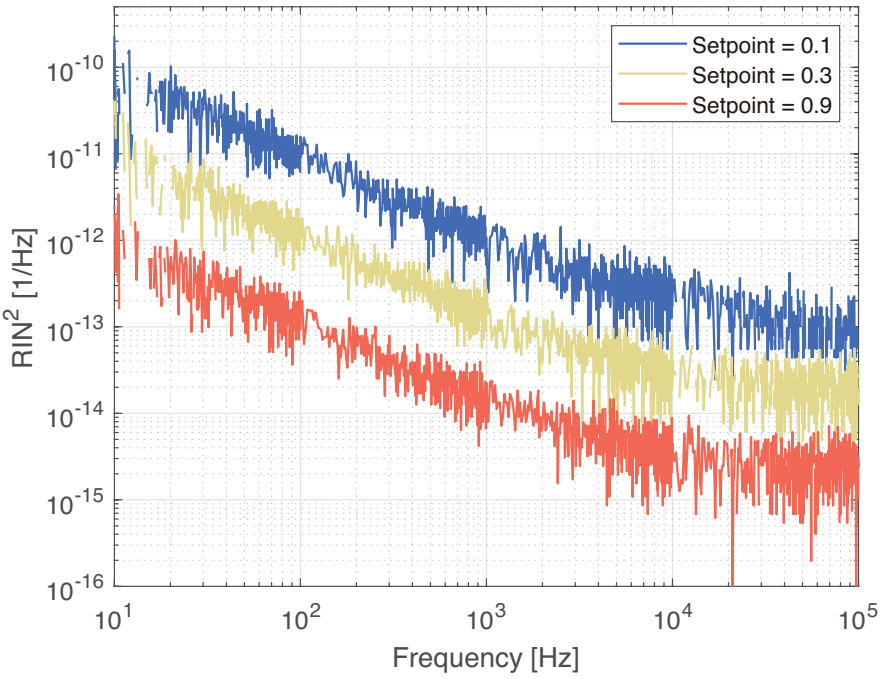

Figure 3.8: RIN spectra of three different setpoints: 0.1 blue curve, 0.3 yellow curve, 0.9 red curve.

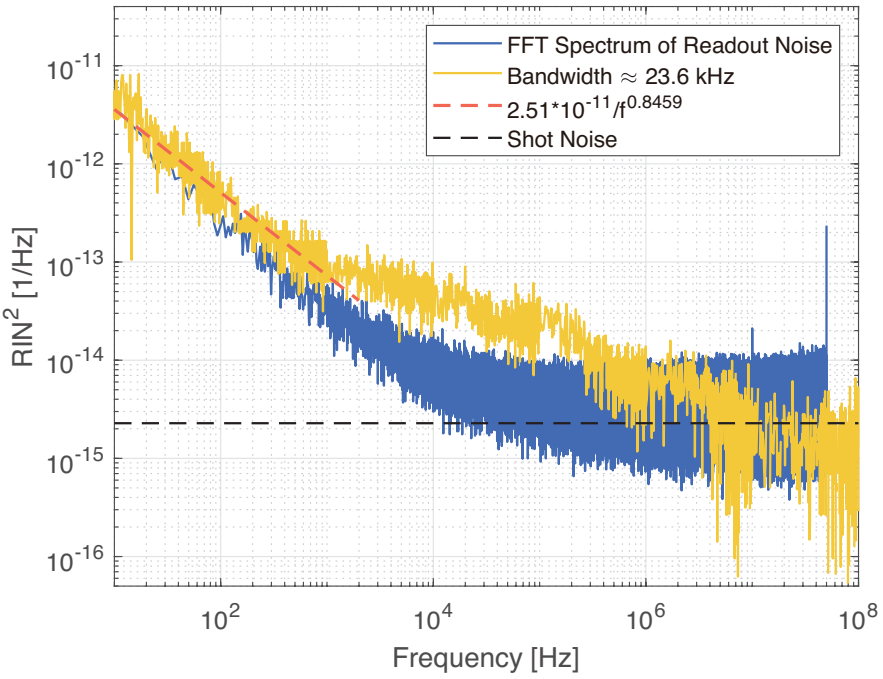

Figure 3.9: Comparison of readout noise and system noise. Yellow curve is the system noise with the bandwidth of 23.6 kHz and blue curve is the readout noise FFT spectrum.

As mentioned in the analysis of readout noise part, by using the Fourier Transform of the ADC readout data, we calculate the readout noise spectrum. To understand its influence on the system, we compare the readout noise with the prototyping system noise. Shown in Fig. 3.9, between 10 Hz and 10^3 Hz, readout noise is the predominant noise source. In the higher frequency, the contribution from readout noise becomes minor.

3.4 Analog Lock Based on Vescent Control Box

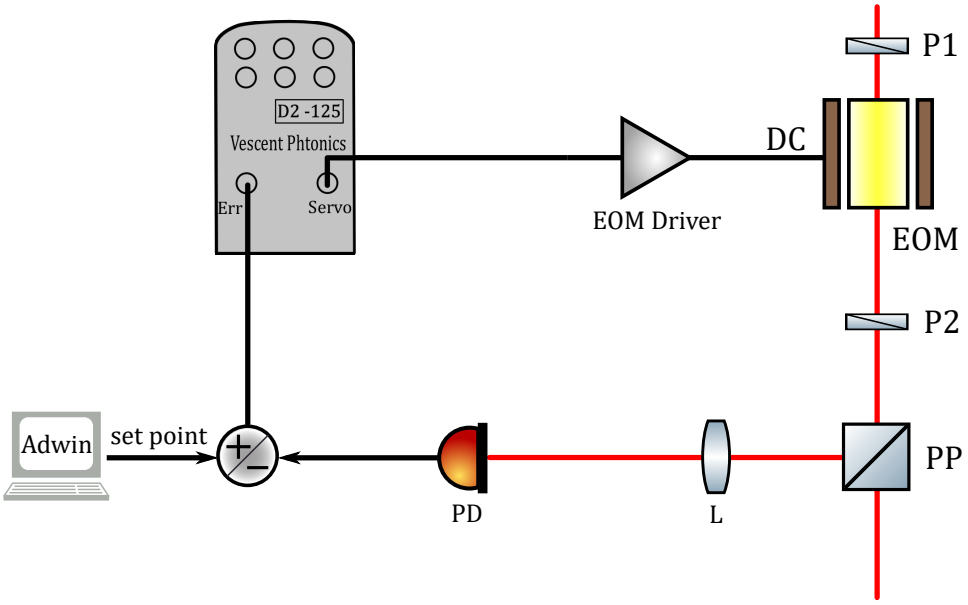

Figure 3.10: Schematics of intensity control system based on EOM intensity modulator. P1: input polarizer, P2: output polarizer, PP: pickup plate, L: focus lens, PD: photodiode.

To compensate the limit of the digital intensity lock bandwidth, we use an analog intensity lock after the TiSa to implement more suppression on the high-frequency noises. The analog intensity lock setup, which is shown in Fig. 3.10, mainly includes the amplitude modulator (P1, P2 and EOM), the Vescent controller, the EOM driver, the adder used to calculate the error signal, the photodiode measuring the optical power and the Adwin output used to provide the setpoint).

As derived in section 2.3.1, the transmission T has a non-linear dependence on EOM voltage V, which means the intensity stabilization system based on EOM is not a linear one. To tune the PIID gains of the Vescent control box, we monitor the step response of the system. A small step stimulus from the setpoint is made. The PIID gains are carefully tuned so that the rise time of the system reaches minimum without inducing an obvious overshooting.

From the step response, shown in Fig. 3.11(a), the time the system needs to stabilize is about 550 ns. To see the noise suppression performance of the analog lock, we measure an in-loop RIN spectrum by splitting half of the signal from the in-loop photodiode to the network analyzer. The measurement result is shown in Fig. 3.11(b). From the measurement, it can be seen that the

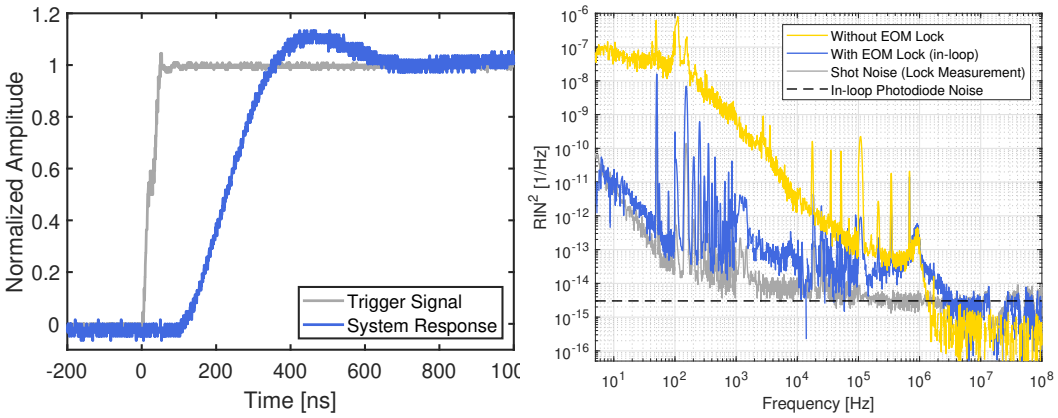

(a) (b)

Figure 3.11: The process to tune the analog system and determine the bandwidth of the system. (a) Step response of the analog intensity lock.Grey curve is the trigger signal of the step, and blue curve is the system step response, (b) the amplitude of system transfer function $H(f)$.

noise peaks at frequencies higher than 200 kHz lower than 1 MHz are effectively suppressed. This frequency range is beyond the reach of digital lock. In the low frequency part, the analog system also has a good performance: noise is suppressed around 100 times. It is also noteworthy that several noisy peaks exist in the frequency domain [50, 10^3] Hz. By comparing the noise spectrum with the photodiode noise background, we can conclude that these noises come from electronics rather than from the beam intensity. During the characterization of the intensity lock, we also make efforts to investigate into the ground loop problem which is suspected to induce the electronic noise in the frequency domain from 50 Hz to several kHz.

3.5 Intensity Noise of Optical Lattice Beam

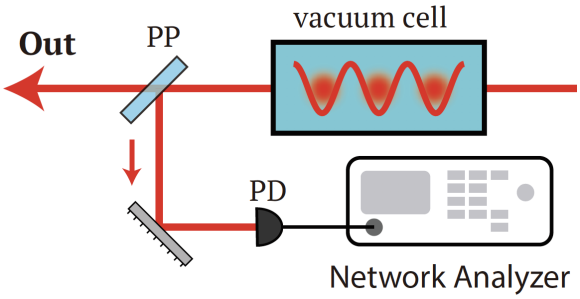

Figure 3.12: Setup for the RIN measurement of lattice beam. Abbreviation: PD: photodiode, PP: pickup plate.

To characterize the RIN of the optical lattice beam, a pickup plate samples a portion of the beam power, which is then measured by an out-of-loop photodiode. Before entering the vacuum

cell, the lattice beam has been stabilized by both the digital intensity lock based on Keysight module and the analog lock based on Vescent control box.

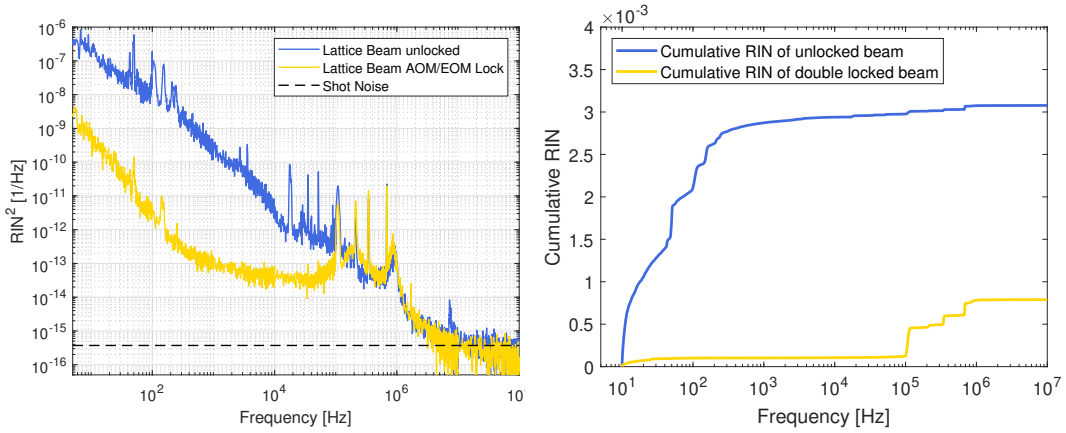

(a) (b)

Figure 3.13: Intensity characterization of the optical lattice beams. (a) RIN spectrum of the lattice beam, (b) the cumulative RIN of the lattice beam. Blue curve represents the scenario where the two intensity locks are disabled, while yellow curve is the scenario where both of the locks are enabled.

From Fig. 3.13, we can conclude the two intensity locks have a strong suppression effect on the intensity noise especially in the low frequency domain. In the frequency interval $[10^2,\ 10^4]$ Hz, the relative noise is reduced more than 100 times. Close to the DC, the relative noise is higher than predicted. Because this abnormality does not appear in the RIN spectrum of analog intensity lock, it is most probably caused by some instability of the system, for example the fiber couplers. In the frequency range close to 1 MHz, the noise is not suppressed due to the limited bandwidth of feedback loop.

3.6 Excursion: Ground Loop Problem

3.6.1 Introduction to Ground Loop Problem

Although the existence of ground loop is well-known, the cause and solution of it are usually a mystery to many people. Ground loop is a condition where an unintended connection to ground is made through an interfering electrical conductor. Generally, ground loop connection exists when an electrical system is connected through more than one way to the electrical ground. During the design of electrical circuits, an absolute ground with zero volt is always assumed. However, when considering the ground loop problems, we have to realize the absolute ground does not exist. There are different electrical resistances between all grounding points in the system. These resistances are dependent with the environment condition, for example, temperature and humidity. When a current flows from the equipment, the resistances yield a voltage difference between different ground points and thus induce noise into the system [28]. These currents can be induced by different reasons:

- In all the real equipment, there are parasitic capacitances between the power line and the equipment ground. They are the unavoidable inter-winding capacitances of its power transformer. These capacitances allow leakage current to flow between power line and ground inside every piece of equipment.

- Voltage differences between outlets' grounds: due to the fact that the different sets of facilities are all connected with grounds, a closed conductive loop is formed through the building utility ground wire. The ambient magnetic fields in the lab passing though the ground loop will induce a current in the loop by electromagnetic induction. In effect, the ground loop acts as a single-turn secondary winding of a transformer, the primary being the summation of all current carrying conductors nearby. When facilities are connected with different outlets, the size of the ground loop can grow large, which makes the system vulnerable to the electromagnetic noises. [29]

The solution of ground loop problem is not easy to find, even though we have understood the mechanism of it. When making attempts to reduce the system noise, we should not sacrifice the grounding safety. Besides, because the networks of different systems vary from one to another, it is unrealistic to create one solution that universally works for every system.

3.6.2 Ground Loop in Intensity Stabilization System

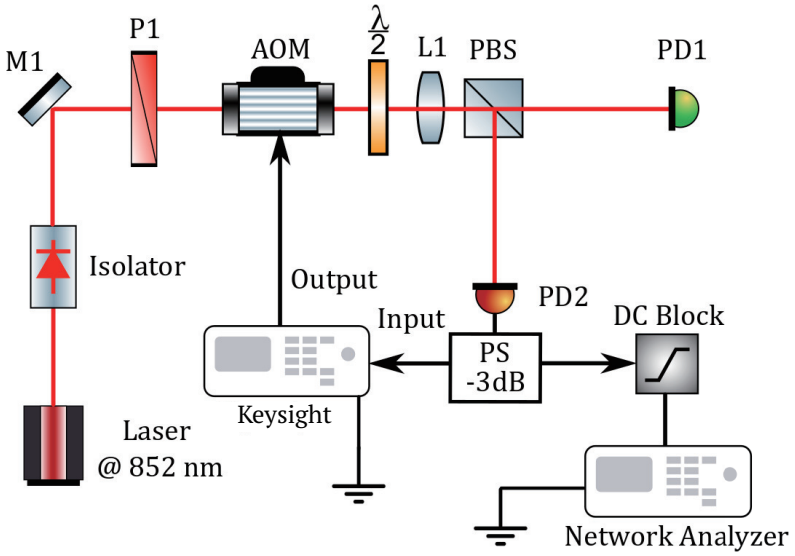

Figure 3.14: Experimental Setup of in-Loop RIN Measurement. Red lines denote the optical path and the black lines denote the electrical connection. PD1: out-of-loop photodiode, PD2: in-loop photodiode, P1: polarizer, $\frac{\lambda}{2}$: half-wave plate, L1: lens used to focus beam at photodiode, PBS: polarized beam splitter, PS: power splitter.

In our digital intensity lock system, ground loop problem also exists. During the in-loop RIN measurement, the Keysight module, power splitter, AOM and the network analyzer form a ground loop, shown in Fig. 3.14. The Keysight module, which has a large amount of digital circuit components compactly integrated together, is a main source of noise.

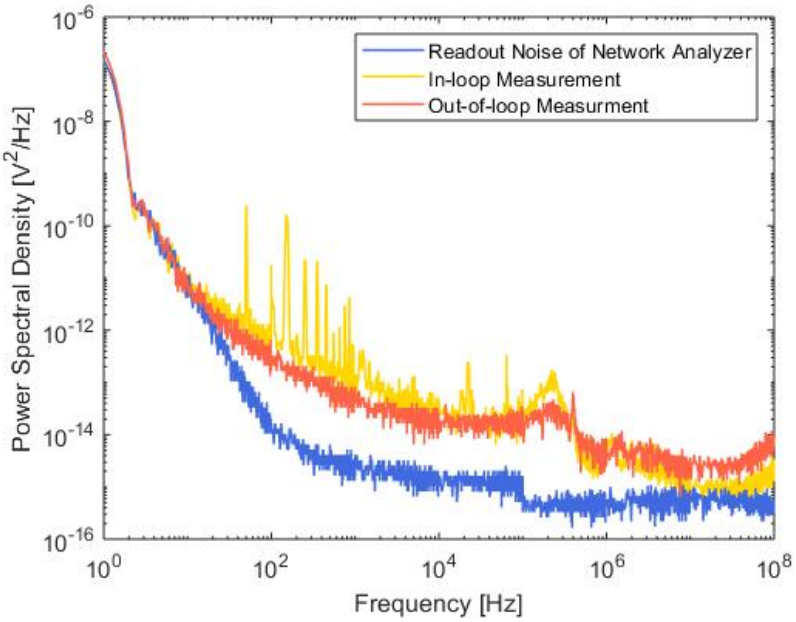

Figure 3.15: Comparison of in-loop and out-of-loop measurement.

In the comparison of the in-loop RIN measurement and out-of-loop RIN measurement, we noticed the out-of-loop measurement has a better RIN curve. In the in-loop measurement noise peaks are found at following frequencies: [50, 150, 250, 350, 450, 550, 650, 750, 850] Hz. Also, in-loop measurement presents a higher noise floor than out-of-loop measurement, which contradicts with the common sense that in-loop measurement always outperforms out-of-loop measurement, because the noises originated from the in-loop detector can be regarded as the process noise and compensated by the controller in the loop.

According to the features of our system, we have take several measures to reduce the influence of ground loops:

- Modifications have been made to the outlet we use: a diode rectifier has been added between the ground line of outlet and the ground ports of sockets, which means the connections between the grounds/chassis of facilities have been safely broken. Only when the voltage difference between chassis and ground is larger than 0.734 V, the connection is bridged. However, it's usually not the case.

- Furthermore, we choose the optical table as our newly defined ground. The modified outlet's ground line is connected with optical table. Grounds of network analyzer and Keysight are linked to the optical table from their front panel's ports. The impedance

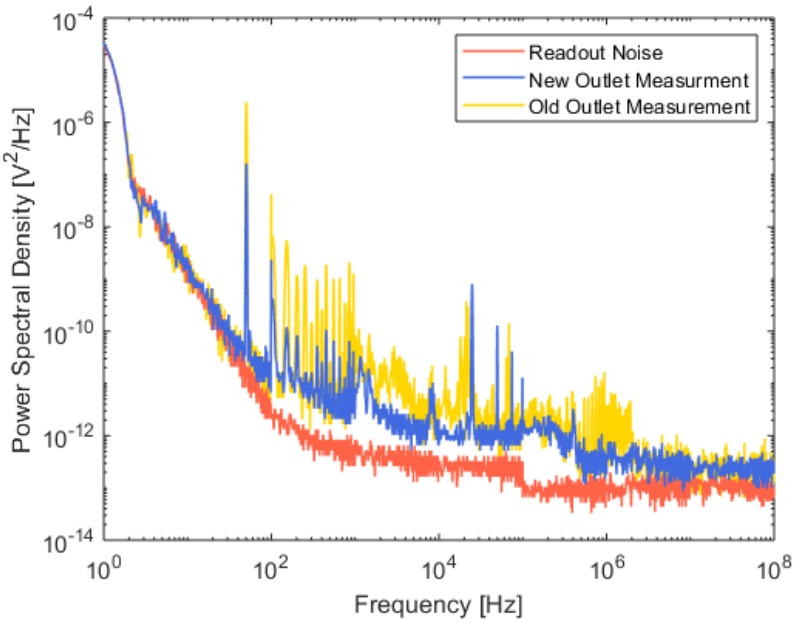

Figure 3.16: Comparison of new outlet and old outlet measurement.

between the facilities' ground and optical table is around 0.2 ohms.

By doing these, we shrink the size of ground loop to decrease the magnetic induction's influence.The noise coming from the power is eliminated, while the safety protection of the equipment is maintained. And with the optical table as the common ground, the negative effects of ground voltage difference should be minimized. From the measurement result, showed in Fig. 3.16, we find the noise floor of the measurement has been lowered, and several noise peaks have disappeared, which suggest an improvement of ground loop problem.

CHAPTER 4

Fast Intensity Modulation Based on Feedforward

In this chapter, I will firstly introduce the idea of our intensity control system based on feedforward. Afterwards, more technical details will be presented, including the linearization of intensity modulator and establishment of AOM process model. To show the advantages of feedforward control, a comparison between our regime and pure feedback loop is made in terms of step response performance.

4.1 Basic Idea: Feedforward

The notion of feedforward, which is a useful complement to feedback, plays an important role in our intensity modulation system. The motivation of using feedforward lies in the pursuit of modulation bandwidth. The feedback control can satisfactorily work against small environmental pertubations, but if a predictable change is going to be applied, one can do better rather than just waiting for the feedback loop to respond.

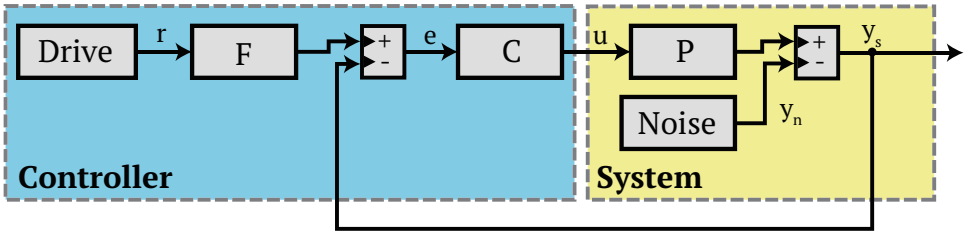

Figure 4.1: The block diagram for the combination of feedback and feedforward control system. C: controller, P: process, F: filter, r: reference signal, y_n: environmental noise, y: system output, e: error signal, u: controller output.

One usual way is to apply a prefilter $F(s)$ to the control signal $r(s)$, shown in Fig. 3.1. Without any feedback loop, the system response signal is $y(s) = F(s)P(s)r(s)$, where $P(s)$ is the system transfer function describing the component dynamics. Given that, if the filter we select is just $F(s) = P^{-1}(s)$, then the system response $y(s)$ would be exactly our control signal $r(s)$.

However, it is usually impossible to just invert $P(s)$, because of the power and bandwidth limit of actuator. But the system dynamical response will still be remarkably improved, if one applies an approximation inverse of $P(s)$ [25]. This means we invert $P(s)$ in the low-frequency domain to the widest extent, and leave the part above a certain cutoff frequency, which is set by actuator limits, unchanged. Furthermore, since the environmental disturbances are usually unknown, it is necessary to combine the feedforward loop with feedback loop. Ignoring the sensor noise, after adding the feedback loop, the system response $y(s)$ becomes

$$y(s) = \frac{CP}{1+CP}[F(s)r(s)] + \frac{1}{CP}y_n(s) \tag{4.1}$$

If we construct $F(s)$ as close to $\frac{CP+1}{CP}$ as possible, then the system response will become

$$y(s) = r(s) + \frac{1}{CP}y_n(s) \tag{4.2}$$

By combing the feedforward and feedback loops, not only does one shape the response as desired, but also effectively suppress the disturbances $y_n(s)$.

4.2 Intensity Control Based on Feedforward

Control theory is most powerful when the controlled object is linear, that is, the proportionality between its response and stimulus is preserved. Without the linearity between system input and output, feedforward control will be difficult to implement. In the case of AOM intensity modulator, by confining the RF signal power to a specific range, we can work in a situation where the diffraction efficiency is monotonically increasing function of RF driving power. Afterwards, we apply a Lookup Table (LUT) inside the Keysight digital platform so that the intensity modulator is a linear one.

The time delay of the digital system has imposed a limit on the feedback loop bandwidth, which suggests modulating the system by feedback loop is not a good option. Inspire by the idea of feedforward, by adding several feedforward loops, we intend to create an equivalent filter $F(s)$ that boosts the modulation up.

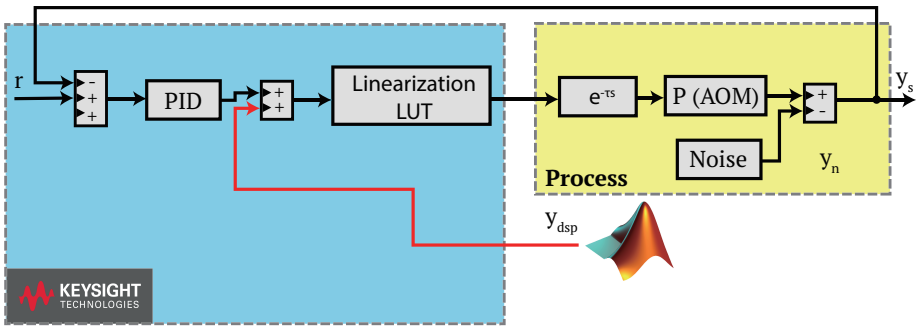

Figure 4.2: Illustration of the feedforward system based on Keysight module: applying the direct setpoint. Abbreviations: P(AOM): the process of AOM, LUT: lookup table, $e^{-\tau s}$: system time delay.

Adding Line 1:

To avoid driving the system by feedback loop, we firstly adds a direct setpoint line to the LUT, which is purposed to apply the modulating signal to the system. However, the consequence of the directly setpoint at system output will be regarded as environmental disturbances by the feedback loop.

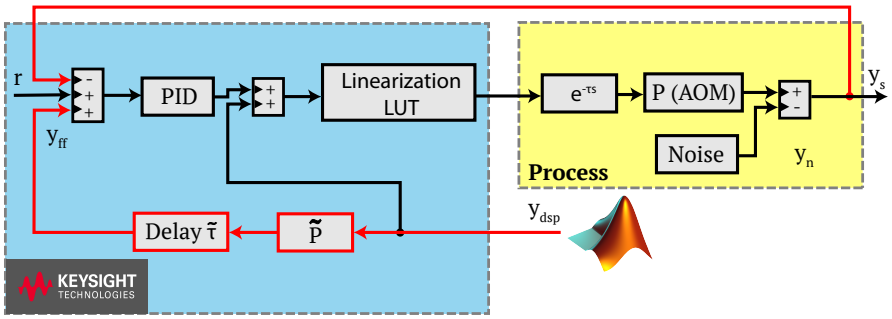

Figure 4.3: Illustration of the feedforward system based on Keysight module: adding feedforward loop to compensate the consequence of the direct setpoint. Abbreviations: y_{ff}: feedforward signal.

Adding Line 2:

In order to counteract the consequence of the direct setpoint, a feedforward loop is created to imitate the system process so that we can predict the system output according to the modulating signal. Then, we subtract the feedforward imitating signal from the feedback signal. If our model of system delay and process is accurate enough, the feedback signal should be well canceled.

From the view of entirety, by adding these two lines, we tailor the system output to be:

$$y_s(s) = e^{-\tau s} P(s) y_{dsp}(s) + \frac{1}{1 + C(s)P(s)e^{-\tau s}} y_n(s) \tag{4.3}$$

The first term represents system's response to the modulating signal and the second term shows the environmental noise suppression.In our experiments, the time sequence is planned in advance. We know very well when the changes will happen beforehand. Thus, the effect of dead time can be well compensated by taking it into consideration during the sequence compiling. Then, the bandwidth of the intensity control system will be limited by the AOM rise time. Furthermore, if a filter of P^{-1} is available and is applied to process the direct setpoint signal $y_{dsp}(s) = e^{\tau s} P^{-1}(s)$, then the output of the system is:

$$y_s(s) = r(s) + \frac{1}{1 + C(s)P(s)e^{-\tau s}} y_n(s) \tag{4.4}$$

If the $P^{-1}(s)$ is available and the model of AOM modulating process is accurate enough, the system output would be just the same with driving signal. However, as mentioned earlier, the

realization of the filter$P^{-1}(s)$ is limited by the hardware. In our experiments, the filter of $P^{-1}(s)$ is not applied.

4.2.1 Linearization of AOM Intensity Modulator

Principle

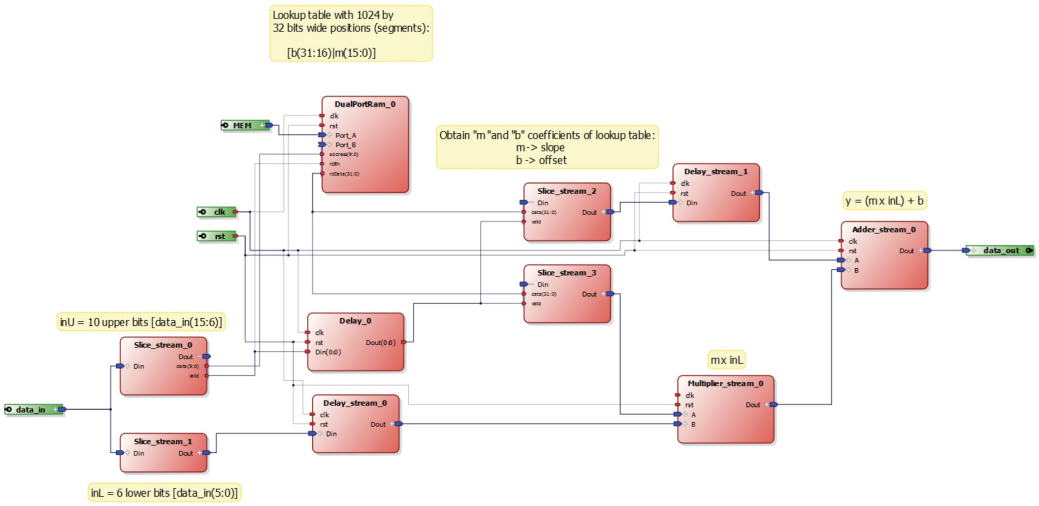

Figure 4.4: Internal diagram of digital LUT[30].

The LUT works as a mapping from input range [0, 1] to output range [0, 1], and is filled with first-order Taylor's polynomial coefficients to implement a piecewise linear approximation of the inverse function of AOM efficiency curve. If we denote the function of AOM diffraction efficiency curve as $\mathrm{P}_{light} = f(\mathrm{P}_{RF})$, then its inverse function, existing because of monotonicity, can be written as $\mathrm{P}_{RF} = f^{-1}(\mathrm{P}_{light})$. When a control signal P_{set} reaches LUT, it is translated into an output of $y_{lut} = f^{-1}(\mathrm{P}_{set})$ according to the written coefficients. After the process of AOM, the output signal will be just the same with input signal: $\mathrm{P}_{light} = f(y_{lut}) = \mathrm{P}_{set}$, which means the combination of LUT and AOM makes a linear component.

The entire input range of LUT is divided into 1024 segments with the length of 2^{-10}. For every segment, a 32-bit data is assigned to record the slope and offset of piecewise linear approximations. The required input of LUT is a 16-bit number, of which the upper 10 bits are used to determine the segment while the lower 6 bits are multiplied by piecewise slope and then added with offset to obtain the 16-bit output number. Due to the fact that the input and the output ranges are both [0, 1], it is necessary to coordinate the signal scales so that the accuracy of LUT can be fully exploited. For instance, before reaching and driving the AOM, the RF signal generated by Keysight is amplified 27 dB, and the input scale of digitizer is carefully set such that maximum light intensity coincides with the input of 1.

During the linearization of intensity modulator, in the first place, the diffraction efficiency curve of AOM is measured, shown in Fig. 4.5(a). As mentioned in last paragraph, the input scale is carefully chosen so that the maximum input corresponds to 1. To adapt to the scheme

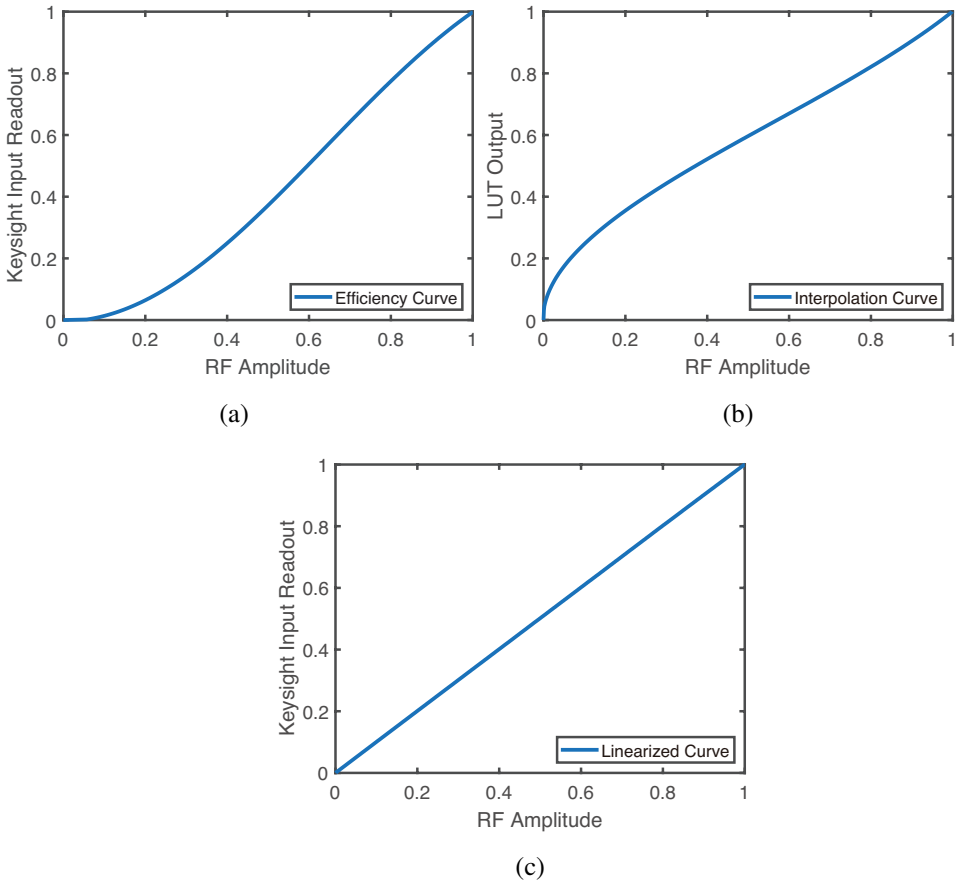

Figure 4.5: Linearization of AOM. (a) Diffraction efficiency curve of AOM. (b) Interpolation function written in LUT. (c) Linear relation between light power and RF signal after applying LUT.

of LUT, the diffraction efficiency curve is cut into 1024 parts, and for each part, the slope and offset are calculated so that we can obtain the piecewise interpolation curve (see in Fig. 4.5(b)). After writing the LUT with linear approximation coefficients, we enable it and measure the new response function, shown in Fig. 4.5(c). Except for the section that is very close to the origin, we successfully limit the maximum relative deviation to be less than 0.4%.

Effects of Laser Power Fluctuation and Drift

As mentioned above, the input scale of digitizer is deliberately chosen so that the maximum beam power corresponds to the input of 1. However, the drift and fluctuation of laser power are inevitable, which lead to a degradation of LUT performance. To evaluate the effect of laser power drift on LUT, we have investigated the short-term and long-term linearity drift of LUT. In a time range of 10 minutes, the maximum relative slope deviation from 1 can reach 1%, while in a sampling survey for 5 days, the maximum drift is 6%.

To avoid the performance degradation, two measures can be taken: 1) stabilize the beam power before AOM intensity modulator, 2) recalibrate the LUT frequently. Power stabilization can

effectively cancel the negative influence of short-term power fluctuation while the recalibration makes the system immune to the effect of long-term power drift.

4.2.2 Modeling of the Process of AOM

Theoretical Model

To implement the feedforward control, we build up a model to imitate the process of AOM $P(s)$ so that the consequence of direct setpoint on feedback loop can be well counteracted. As seen in Fig. 2.6, the time response of AOM includes two characteristic times: dead time ($0 \rightarrow t_1$) and rising time ($t_1 \rightarrow t_2$).

The principle of AOM intensity modulation is the interaction of sound wave existing in crystal and the light passing through the crystal. Thus, the deadtime can be understood as the time interval between the generation of sound wave and the arrival of the sound wave at the beam position. When the sound wave propagates through the beam of TEM_{00} transverse Gaussian mode, the time response function should also be a Gaussian. Therefore, as the convolution of a Gaussian and a Heaviside function, the rising part of the AOM time response can be well fitted by an error function.[18]

The dead time is a pure delay and can be easily handled by Keysight together with delays of other loop components (e.g. the digital cirtuits in Keysight). To imitate the rising part of AOM, a Gaussian has a tunable full width at half maximum (FWHM) is used.

Tuning of Modeling Parameters

The model we developed to describe the process of AOM including two tunable parameters: time delay t_d and convoluting width ω_c. To determine the optimal parameters, we implement several step response tests with different combinations of the two parameters. In these tests, we apply a step change at the direct setpoint y_{dsp} without using the deconvolution algorithm to prepare the setpoint data. In this way, the suitability of the convoluting width is reflected by the quality of compensation signal. The reasons to use step response include:

- A steep step change is a harsh test for control system. The Laplace transform of a Heaviside step is $\hat{H} = 1/s$, suggesting it contains all frequency components.
- Step response experiments are easy to implement. And theoretical step response function is easy to derive.

In order to evaluate the performance of different combinations of parameters, we defined a new quantity $D(\omega_c, t_d)$ denoting the deviation from a perfect step response. It is the relative mean absolute difference:

$$D = \frac{\sum_{i=1}^{n} |y_{step}(i) - y_{exp}(i)|}{\sum_{i=1}^{n} y_{step}(i)} \tag{4.5}$$

where y_{step} denotes the perfect step response and y_{exp} is the experimental data. Shown in Fig. 4.7, the deviation we defined is proportional to the area of green patch, which quantifies the

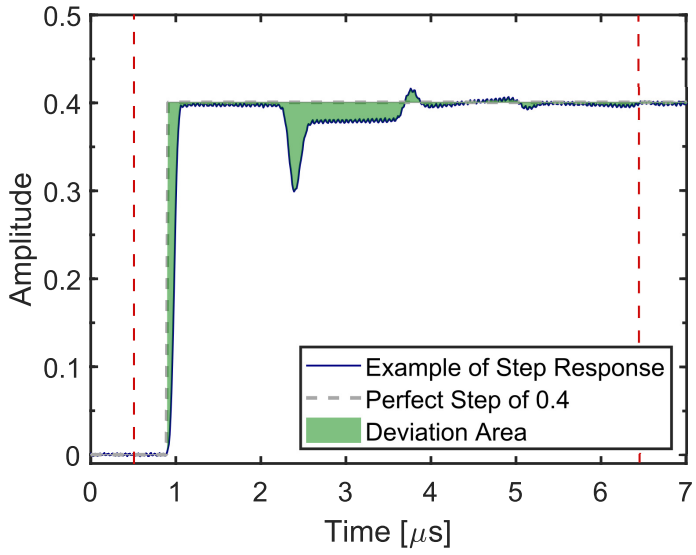

Figure 4.6: Illustration of the evaluation of deviation from ideal step response. Red dash line denotes the boundaries of calculation interval. The Green filled area is the deviation part.

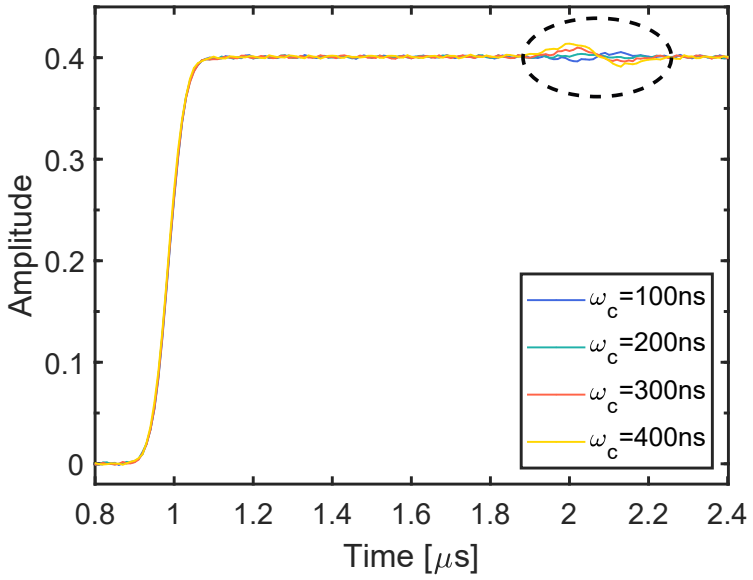

Figure 4.7: Examples of step response during the tuning of two model parameters: t_d and ω_c. Inside the black dotted bordered ellipse are the wiggles caused by the tuning error.

difference between the perfect response and real response. Thus, the combination of parameters leading to the minimum of D corresponds to the optimal setting.

It should be noted, with the step size increasing, the system becomes more sensitive to the two tuning parameters. If the step size is too large, a small difference of tuning parameters from optimal value can lead to an oversize accumulation of error signal, more than what the PI controller can handle. During the scan over parameters, we chose a step size of 0.4. If the

system is well tuned, the maximum step the system can sustain is around 0.9 before going unstable, which suggests a solid system stability.

When the t_d or ω_c is wrongly tuned, a drastic drop or rise appears in the response curve. If the compensation signal is sent too early and it arrives at the summation point before the feedback signal y_s caused by y_{dsp}, it is equivalent to an increase of the setpoint y_{sp}. Therefore, an extra increase will happen in the system response. In the other way around, if the compensation comes late, without cancellation, the feedback signal caused by $y_d sp$ leads to a counteraction of the PI controller. As a result, a drop occurs in the system response, seen in Fig. 4.6. Due to the system delay, the drop and rise will cause a fluctuation of the system. The time difference between the drop (rise) and the fluctuation is exactly the delay of the system.

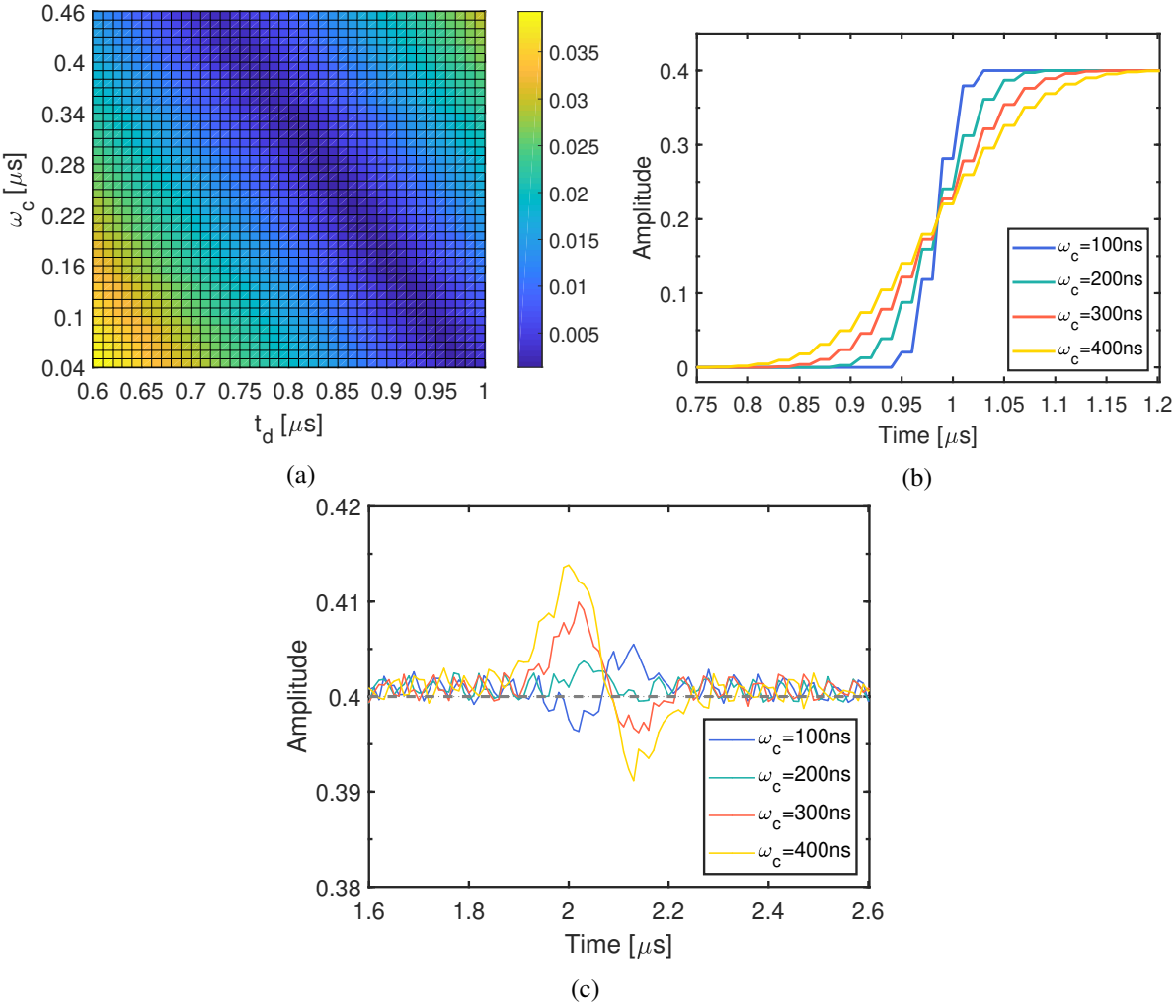

Figure 4.8: (a) During the tuning, a 2D scan over time delay and convoluting width is measured. The gradation of color represents the amount of deviation $D(\omega_c, t_d)$. (b) The compensation pin waveforms along the deep blue direction in graph (a). (c)The zooming-in picture of step responses with different tuning parameters located in the deep blue direction in graph(a).

If the two parameters are well-tuned, the response curve will only have small wiggles shown

inside the dotted bordered ellipse in Fig. 4.7. The quality of feedforward is revealed by the amplitude of these wiggles.

To find the optimal combination of time delay t_d and convoluting width ω_c, we implement a two-dimensional scan over those parameter. The internal 100 MHz reference clock of Keysight allows a delay tuning precision of 10 ns, meanwhile, the 50 MHz AWG determines the tuning precision of convoluting width to be 20 ns. It should be clarified, the maximum sampling frequency of the AWGs can reach 500 MHz at its maximum. However, with the higher sampling frequency, the same duration waveform will cost more storage of the on-board RAM. For the compensation waveform, we scale down the AWGs sampling frequency to be 1/10 of maximum.

The deep blue line in Fig. 4.8(a) suggests the control system tends to have a better performance if the summation of two tuning parameters is greater than 1000 ns and less than 1100 ns. Further looking at the deep blue line, we discover the deviation reaches minimum with $t_d = 870$ ns and $\omega_c = 220$ ns. The minimum relative average deviation $D(\omega_c = 220 \text{ ns}, t_d = 870 \text{ ns})$ is 0.23%.

To investigate the cause of deep blue line, we plot the compensation waveform along the line: $t_d + \omega_c = 1090$ ns. It can be observed from Fig. 4.8(b), all compensation waveforms coincide on the half maximum point of Gaussians. We can infer that the position of the common intersection point is determined by the summation of t_d and ω_c. The deviation decreases evidently with this intersection point approaching the real half maximum point, which results in the concentrated distribution of low-deviation combinations near the deep blue line in Fig. 4.8(a). Afterwards, the performance of those combinations sharing the same half point will be distinguished by their convoluting widths. It can be observed from Fig. 4.8(b) and 4.8(c), when the convolution width is too wide, like the yellow curve, the compensation rises fast in the part before half point resulting an overcompensation, which corresponds to the rise after a system delay time. And after the half point continues rising in a slow manner resulting in the drop afterwards. With the convoluting width approaching the real one, the amplitude of wiggle decreases.

It should also be noticed, in the Fig. 4.8(c), the system output amplitude is very close to 0.4 level as desired. This is an evidence of a nice linearization of intensity modulator, because during that interval, the feedback loop is not quick enough to help the system stabilize. Thus if the quality of linearization is not good, a notable deviation from 0.4 signal level would appear.

4.3 Comparison: Feedback VS Feedforward

Since the process is optimally tuned, we make a step response comparison to exhibit the advantages of feedforward control over feedback control. It can be observed from the Fig. 4.9 that feedforward control evidently boost the response speed of the system. As for the rising time from the zero level to 0.4 level, the feedback system takes 2460 ns, while the feedforward regime only takes 210 ns. The bandwidth of the feedforward control system is estimated to be around 3 MHz. With finely tuned parameters, the disturbance induced by the difference between model and real system is well controlled. Fig. 4.8(b) shows the disturbances with different convolution width setting, and the maximum deviation in optimal situation is less than 0.4%.

Enjoying the advantages of feedforward control, the PID controller does not need to undertake the task of driving the system according to steering signal. Therefore, we have enough leverage to choose the bandwidth of feedback system. It is possible that over some high frequency

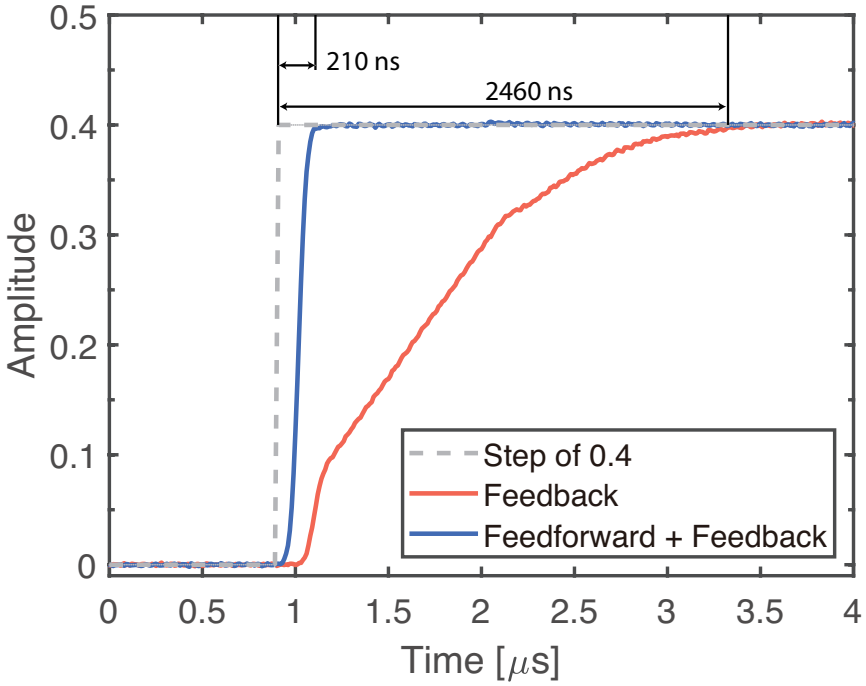

Figure 4.9: Step response comparison between feedback and feedforward system. Blue curve is the step response with both feedforward and feedback loop. Red curve is the step response with only feedback loop. Gray curve is a perfect 0.4 step.

domain, the readout noise is even larger than the other part. Then, with a lower bandwidth, even though part of the noise cannot be suppressed by the feedback loop, the larger high-frequency readout noise is excluded from the output. The lowering of the bandwidth is realized by reducing the P, I, D gains of the PID controller.

CHAPTER 5

Outlook

5.1 Application of Fast Intensity Modulation

As presented in Chapter 4, by using the feedforward regime based on FPGA platform, we achieve an intensity modulation bandwidth of 3 MHz. This technique can be generally applied to many research fields which have high-speed requirement on optical intensity modulation. Quantum Optimal Control (QOC) is one of them.

Nowadays, most quantum manipulation protocols developed so far in research laboratories rely on analytic or simple empirical solutions and are far from being optimal. Therefore it is meaningful to invent a method to design fast and arbitrary complex manipulations. QCC has been proposed and successfully applied to both few-body and many-body systems[31]. As for the system with optical lattices, optical lattice depth is an important parameter to manipulate during the design of manipulation sequence. The feedforward control regime can provide us with the probability to achieve faster robust quantum manipulations.

5.2 Correlation between Intensity Noise and Coherent Time of Atoms

It is well-known that the intensity noise of the optical lattice beam undermines the coherence of the trapped atoms, and theoretical model has been established to describe this decoherence process[6]. However, not many experimental attempts have been done about the topic. The intensity stabilization system provides us the ability to artificially add more noise into the system, for example, by lowering the dynamic range of digital intensity lock. The Ramsey analysis of the atoms trapped in optical with different intensity noises can be implemented to characterize the decoherence time of atoms. The experimental results can give us more insights into the intensity decoherence regime.

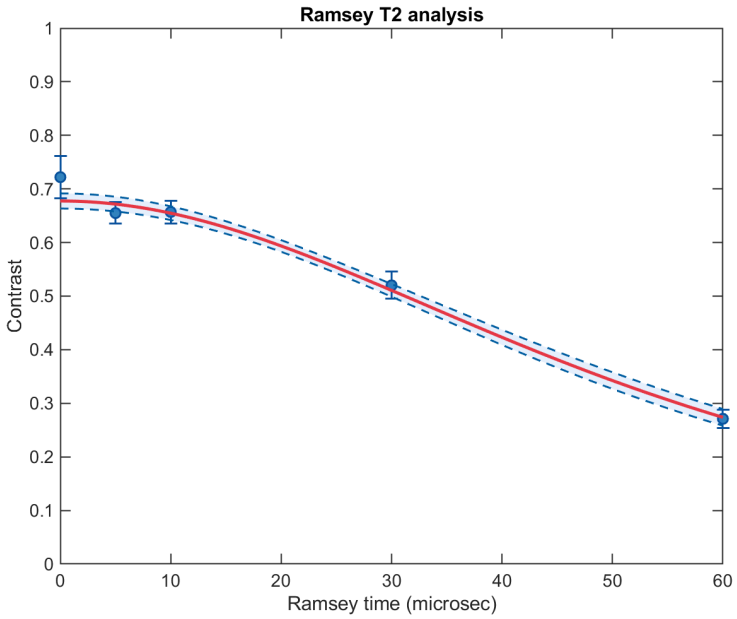

Figure 5.1: Ramsey analysis of atoms trapped in 2D optical lattices.

5.3 Speeding up of Intensity Modulation

The bandwidth of the feedforward intensity modulation can be further boosted, if we apply a deconvolution algorithm to process the modulating signal. At present, the bandwidth is limited by the rise time of the AOM. Since we have successfully built up a Gaussian time response model to imitate the process of AOM, the information of the AOM process can help us design a filter of $P^{-1}(s)$. After applying this filter to the driving signal before input, the system output will exactly follow the driving signal:

$$y_s(s) = r(s) + \frac{1}{1 + C(s)P(s)e^{-\tau s}} y_n(s) \tag{5.1}$$

Due to the limitation of AWG bandwidth and output amplitude, the filter may not be perfect. But the system dynamical response will still be remarkably improved, if we successfully invert $P(s)$ in low-frequency domain.

Acknowledgements

It is an unforgettable year that I spent working in Professor Meschede's outstanding research group. I am honored to learn from and work with a group of excellent scientists and colleagues who make my experience of master thesis project so memorable. Not only do I have the chance to be a member of the team implementing the cutting-edge experiments of quantum simulation, but I also receive so much care and warmth in both of my work and life.

First of all, I would like to thank Professor Meschede for providing me with such a precious opportunity to work and study in his outstanding group. As the group leader and my supervisor, he is always supportive and accessible even though he shoulders a number of administrative and research tasks, which I appreciate very much. And I want to thank Professor Stefan Linden for kindly serving as the second referee of my thesis. I also benefit a lot from attending his class of "Photonic Devices".

I want to express my sincere gratitude to Dr. Andrea Alberti, who gives me this intriguing master thesis topic at the first place. It still impresses me a lot, every time I came to him with a problem (sometimes even very basic problems), he was always enthusiastic to offer his guidance. As the principle investigator, he manages many different research projects in the same time, but he would still spend time working with me in the laboratory side by side.

I would like to thank Dr. Wolfgang Alt, who is always responsive to all kinds of questions I have asked. He has given me many useful suggestions on my projects and presentations. I especially appreciate his serious and rigorous attitude towards research work, from which I have learned a lot.

I want to thank Max, Gautam and Richard, who are both friendly colleagues and good teachers for me. I have learned plenty of experimental techniques and programming skills from them. During the time of difficulties, they always give me comfort and valuable advice. I really enjoy the time we spent in the laboratory together.

I also want to thank Weiqi, Natalie, Manolo and Thorsten, who not only share the same office but also many snacks and stories with me. Every time I turn to them, they always spare no efforts to offer their help. Sitting in the same office with them is a pleasant and enjoyable experience to me.

There are many other group members who I have spent a lot of time with. I very appreciate their friendliness and kindness. And I want to thank my classmates and friends in Bonn, who make my life in Germany colorful and exciting.

At last, I want to thank my family and my girl friend Hedanqiu Bai for always supporting me with all their strength, and for their full understanding of my pursuit of scientific research, without which I would not have such a nice environment to study abroad.

Bibliography

[1] A. M. Childs, L. J. Schulman and U. V. Vazirani,
"Quantum Algorithms for Hidden Nonlinear Structures",
Foundations of Computer Science, 2007. FOCS '07. 48th Annual IEEE Symposium on,
2007 395 (cit. on p. 1).

[2] H. Schmitz et al., *Quantum Walk of a Trapped Ion in Phase Space*,
Physical Review Letters **103** (2009) (cit. on p. 1).

[3] M. Karski et al., *Quantum Walk in Position Space with Single Optically Trapped Atoms*,
Science **325** (2009) 174, ISSN: 0036-8075,
eprint: http://science.sciencemag.org/content/325/5937/174.full.pdf,
URL: http://science.sciencemag.org/content/325/5937/174 (cit. on p. 1).

[4] A. Peruzzo et al., *Quantum Walks of Correlated Photons*, Science **329** (2010) 1500,
ISSN: 0036-8075,
eprint: http://science.sciencemag.org/content/329/5998/1500.full.pdf,
URL: http://science.sciencemag.org/content/329/5998/1500 (cit. on p. 1).

[5] D. S. Weiss and M. Saffman, *Quantum computing with neutral atoms*,
Physics Today **70** (2017) 45, ISSN: 00319228, arXiv: 9904010v1 [arXiv:quant-ph]
(cit. on p. 1).

[6] A. Alberti et al., *Decoherence models for discrete-time quantum walks and their application to neutral atom experiments*, New Journal of Physics **16** (2014) 123052
(cit. on pp. 1, 3, 39).

[7] S. Brakhane, *The Quantum Walk Microscope*, (2016) (cit. on p. 2).

[8] T. Groh et al., *Robustness of topologically protected edge states in quantum walk experiments with neutral atoms*, Physical Review A **94** (2016) (cit. on p. 2).

[9] C. Robens, *Testing the Quantumness of Atom Trajectories*, (2017) (cit. on pp. 2, 3).

[10] A. Steffen, *Single atom interferometers and Bloch oscillations in quantum walks*, (2013)
(cit. on p. 2).

[11] C. Foot, *Atomic Physics*, Oxford Master Series in Physics, OUP Oxford, 2005,
ISBN: 9780198506959,
URL: https://books.google.com/books?id=%5C_CoSDAAAQBAJ (cit. on p. 2).

[12] R. Grimm, M. Weidemüller and Y. B. Ovchinnikov,
Optical Dipole Traps for Neutral Atoms,
Advances in Atomic, Molecular and Optical Physics **42** (2000) 95, ISSN: 1049250X,
arXiv: 9902072 [physics] (cit. on p. 3).

[13] I. Bloch, *Ultracold quantum gases in optical lattices*, Nature Physics **1** () 23 EP,
URL: http://dx.doi.org/10.1038/nphys138 (cit. on p. 3).

[14] S. Kuhr et al., *Analysis of dephasing mechanisms in a standing-wave dipole trap*,
Phys. Rev. A **72** (2 2005) 023406,
URL: https://link.aps.org/doi/10.1103/PhysRevA.72.023406 (cit. on p. 3).

[15] A. Alberti et al., *Atomic wave packets in amplitude-modulated vertical optical lattices*,
New Journal of Physics **12** (2010) 065037,
URL: http://stacks.iop.org/1367-2630/12/i=6/a=065037 (cit. on p. 3).

[16] T. Stöferle et al.,
Transition from a Strongly Interacting 1D Superfluid to a Mott Insulator,
Phys. Rev. Lett. **92** (13 2004) 130403,
URL: https://link.aps.org/doi/10.1103/PhysRevLett.92.130403
(cit. on p. 3).

[17] Keysight, *Keysight M3300A Data Sheet*, (2017) (cit. on p. 7).

[18] M. Werninghaus,
Controlling atom transport in a two-dimensional state-dependent optical lattice,
Master Thesis, Univesity of Bonn (2017) (cit. on pp. 10, 11, 34).

[19] Isomet, *AN0510 Acousto-Optic Modulation*, Application Note **16** (2003) 446,
ISSN: 01419331, arXiv: arXiv:1503.07998v1, URL: www.ISOMET.com (cit. on p. 10).

[20] D. Meschede, "Light Propagation in Matter: Interfaces, Dispersion, and Birefringence",
Optics, Light, and Lasers, Wiley-Blackwell, 2017, chap. 3 83, ISBN: 9783527685486,
eprint:
https://onlinelibrary.wiley.com/doi/pdf/10.1002/9783527685486.ch3,
URL:
https://onlinelibrary.wiley.com/doi/abs/10.1002/9783527685486.ch3
(cit. on p. 11).

[21] T. A. Maldonado, *Handbook of Optics, Chapter 13*, ed. by M. Bass et al.,
McGRAW-HILL, INC., 2004 15, ISBN: 0071498893, arXiv: arXiv:1011.1669v3
(cit. on pp. 11, 12).

[22] Vescent Photonics, *Reconfigurable Laser Servo D2-125*, (2015) 1 (cit. on p. 12).

[23] A. Alberti et al., *Decoherence models for discrete-time quantum walks and their application to neutral atom experiments*, New Journal of Physics **16** (2014) 123052,
URL: http://stacks.iop.org/1367-2630/16/i=12/a=123052 (cit. on p. 13).

[24] M. Araki, *PID control*, Control systems, robotics and automation 2 **II** (2002) 1
(cit. on p. 14).

[25] J. Bechhoefer, *Feedback for physicists: A tutorial essay on control*, Rev. Mod. Phys. **77** (3 2005) 783, URL: https://link.aps.org/doi/10.1103/RevModPhys.77.783 (cit. on pp. 14, 30).

[26] R. Paschotta, *Understanding Intensity Noise*, Encyclopedia of Laser Physics and Technology (2018), Wiley-VCH, ISSN: 9783527408283 (cit. on p. 15).

[27] W. Kester, *ADC Input Noise: The Good, The Bad, and The Ugly. Is No Noise Good Noise?*, Analog Dialoge **40** (2006) 1 (cit. on p. 19).

[28] T. Engdahl, *Ground loop problems and how to get rid of them*, Communications (2000) (cit. on p. 25).

[29] C. C. Est and B. Whitlock, *Eliminating Ground Loops*, (1995) (cit. on p. 26).

[30] K. Technologies, *FPGA Implementation of a LUT-Based Input Processing Using M3602A FPGA Design Environment* (cit. on p. 32).

[31] S. van Frank et al., *Optimal control of complex atomic quantum systems*, Scientific Reports **6** (2016) (cit. on p. 39).